

CO DEPLETION IN PROTOPLANETARY DISKS: A UNIFIED PICTURE COMBINING PHYSICAL SEQUESTRATION AND CHEMICAL PROCESSING

SEBASTIAAN KRIJTT^{1,5,7}, ARTHUR D. BOSMAN², KE ZHANG^{2,5}, KAMBER R. SCHWARZ^{3,6}, FRED J. CIESLA^{4,7} & EDWIN A. BERGIN²

Draft version July 21, 2020

ABSTRACT

The gas-phase CO abundance (relative to hydrogen) in protoplanetary disks decreases by up to 2 orders of magnitude from its ISM value $\sim 10^{-4}$, even after accounting for freeze-out and photo-dissociation. Previous studies have shown that while local chemical processing of CO and the sequestration of CO ice on solids in the midplane can both contribute, neither of these processes appears capable of consistently reaching the observed depletion factors on the relevant timescale of 1–3 Myr. In this study, we model these processes simultaneously by including a compact chemical network (centered on carbon and oxygen) to 2D ($r+z$) simulations of the outer ($r > 20$ au) disk regions that include turbulent diffusion, pebble formation, and pebble dynamics. In general, we find that the CO/H₂ abundance is a complex function of time and location. Focusing on CO in the warm molecular layer, we find that only the most complete model (with chemistry and pebble evolution included) can reach depletion factors consistent with observations. In the absence of pressure traps, highly-efficient planetesimal formation, or high cosmic ray ionization rates, this model also predicts a resurgence of CO vapor interior to the CO snowline. We show the impact of physical and chemical processes on the elemental (C/O) and (C/H) ratios (in the gas and ice phases), discuss the use of CO as a disk mass tracer, and, finally, connect our predicted pebble ice compositions to those of pristine planetesimals as found in the Cold Classical Kuiper Belt and debris disks.

Subject headings: protoplanetary disks — astrochemistry — stars: circumstellar matter — methods: numerical

1. INTRODUCTION

The carbon-monoxide (CO) molecule has played an important role in our understanding of protoplanetary disks. Being abundant, volatile, and having rotational transitions readily observable at millimeter wavelengths, emission from gas-phase CO and its isotopologues has been used to study, amongst other things, disk sizes (Andrews et al. 2012; Ansdell et al. 2018; Trapman et al. 2019; Boyden & Eisner 2020), gas masses (Ansdell et al. 2016; Miotello et al. 2016), temperature profiles (Zhang et al. 2017; Dutrey et al. 2017; Dullemond et al. 2020), as well as detailed gas kinematics and their relation to turbulence (Flaherty et al. 2015; Teague et al. 2016) and the presence of planets (e.g., Teague et al. 2018; Pinte et al. 2019).

While the abundance of CO (relative to hydrogen) is generally $\sim 10^{-4}$ in the ISM and molecular clouds, a picture is beginning to emerge in which CO becomes increasingly depleted in the warm ($T \gtrsim 20$ K) molecular layers of protoplanetary disks (Bergin & Williams 2017); regions in which CO should be unaffected by freeze-out

or photo-dissociation (Williams & Best 2014).

First, many disks are surprisingly faint in CO emission (Eisner et al. 2016), which results in low estimates for disk gas masses (Ansdell et al. 2016; Miotello et al. 2017; Long et al. 2017). Furthermore, in sources for which an independent measure of the hydrogen gas mass exists in the form of HD, CO abundances as low as 10^{-6} have been reported (Favre et al. 2013; Bergin et al. 2013; McClure et al. 2016). Recently, Zhang et al. (2020b), by contrasting observations of multiple class 0/I and class II disks, found that CO depletion factors of 10–100 are common, and appear to be established on timescales of ~ 1 –3 Myr (see also Bergner et al. 2020).

Understanding the mechanism(s) behind the removal of CO is important for several reasons. First, the accuracy of using CO emission as a gas mass tracer relies on a firm understanding of what CO/H₂ should be. Second, CO is an important carrier of carbon and oxygen, so if the underlying mechanism (whatever it is) will change the molecular and/or elemental abundances in the disk, affecting the compositions of (giant) planets forming there (e.g., Öberg et al. 2011; Öberg & Bergin 2016; Booth et al. 2017; Eistrup et al. 2018; Cridland et al. 2019, 2020).

Several authors have studied chemical CO processing as the source for the inferred depletion (e.g., Aikawa et al. 1996; Bergin et al. 2014; Reboussin et al. 2015; Bosman et al. 2018b; Schwarz et al. 2018; Dodson-Robinson et al. 2018; Schwarz et al. 2019). Using passive model disks (i.e., ignoring material transport), these authors generally find that chemical processing alone is inefficient on \sim Myr timescales in regions of the disk where CO is

skrijt@email.arizona.edu

¹ Department of Astronomy/Steward Observatory, The University of Arizona, 933 North Cherry Avenue, Tucson, AZ 85721, USA

² University of Michigan, Department of Astronomy, 1085 S. University, Ann Arbor, MI 48109, USA

³ Lunar and Planetary Laboratory, University of Arizona, 1629 E. University Blvd, Tucson, AZ 85721, USA

⁴ Department of the Geophysical Sciences, The University of Chicago, 5734 S. Ellis Avenue, Chicago, IL 60637, USA

⁵ Hubble Fellow

⁶ Sagan Fellow

⁷ EOS Team, NASA Nexus for Exoplanet System Science

not frozen out. Models with cosmic ray ionization rates $\zeta_{\text{CR}} \gtrsim 10^{-17} \text{ s}^{-1}$ can produce significant depletion factors in some cases (Bosman et al. 2018b), but become inefficient in warmer disk regions, in disks with a significant amount of mass in pebble-size particles, and for low oxygen abundances (Schwarz et al. 2018). Furthermore, it is unclear how appropriate ISM-level values for ζ_{CR} are inside protoplanetary disks (Cleeves et al. 2015).

Alternatively, others have considered physical sequestration of CO in the cold ($\lesssim 20\text{K}$) outer disk midplane, often requiring of vertical transport with either grain growth (e.g., Kama et al. 2016; Krijt et al. 2018), or a vertically-varying diffusion coefficient (Xu et al. 2017). A natural by-product of models that rely on dust coagulation and transport is that, in the absence of chemical processing, the inward radial drift of icy pebbles will increase the gas-phase CO abundance interior to the CO snowline, in some cases by an order of magnitude (Piso et al. 2015; Stammerl et al. 2017; Krijt et al. 2018).

Recently, Zhang et al. (2019) inferred radially resolved CO depletion profiles for a handful of nearby disks (DM Tau, TW Hya, HD 163296, and IM Lup), concluding that while the radial variations in the CO abundance are similar to those predicted by Krijt et al. (2018), the observed depletion factors can be significantly higher than those found in the simulations, suggesting that *both* ongoing chemical processing and dust evolution and transport play a role in setting the CO abundance. For HD 163296, the only case in which the region interior to the midplane CO snowline could be resolved, evidence for an increased CO abundance in the inner regions was found, and later confirmed using additional observations (Zhang et al. 2020a).

While theoretical studies have started to combine physical and chemical evolution (Booth et al. 2017; Bosman et al. 2018a; Booth & Ilee 2019), most of these works focused on the effect of inward radial transport on molecular abundances in the disk midplane, thus limiting their models to 1D without discussing the warm molecular layer.

We set out to study how processes associated with the earliest stages of planet/planetesimal formation (i.e., the formation of pebbles, their accumulation in the midplane, and their subsequent inward migration) interact with ongoing chemical processing of CO (through either gas-phase or grain-surface reactions). Our main goal is to explore whether these processes, acting together, can explain the extreme CO depletion factors, as well as their radial variations, that have been reported in the literature (e.g., Zhang et al. 2019, 2020b), establishing a direct link between observational constraints probing the outer disk surface layers to physical and chemical processes taking place in the less accessible disk midplane.

2. METHODS

We summarize here the various chemical and physical processes that are considered.

2.1. Disk structure

In this work, we focus on the region exterior to $r = 20$ au, as we are interested in the behavior around and outside the CO snowline. When setting the disk gas 2D density and temperature structure (both assumed constant in time) we use the same approach as detailed in

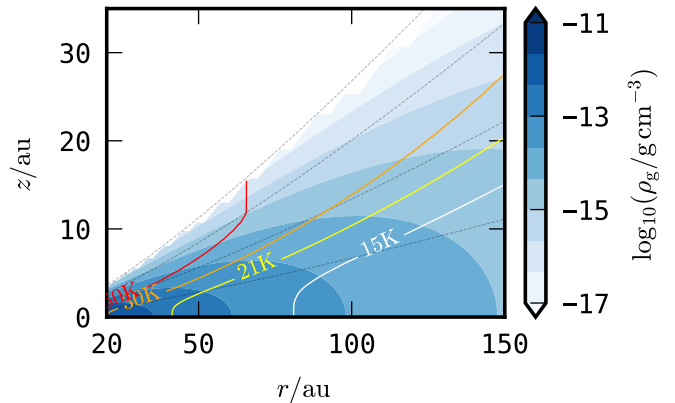


FIG. 1.— Gas density and temperature structure used throughout this study (see Sect. 2.1). Dashed lines indicate $z/H = \{1, 2, 3, 4\}$.

Krijt et al. (2018, Sect. 2.1), with minor changes to some of the global disk parameters. Specifically, focusing on a disk around a sun-like star, we have set the characteristic disk radius $r_c = 80$ au, disk mass $M_{\text{disk}}/M_{\star} = 0.1$, and the midplane temperature $T_{1\text{au}} = 135$ K, making the disk slightly smaller, twice as massive, and a little bit warmer compared to the one in Krijt et al. (2018). The gas density and temperature structure is illustrated in Fig. 1.

At $t = 0$, we assume all grains are $0.1 \mu\text{m}$ in size, and present everywhere in the disk at a dust-to-gas mass ratio of $(\rho_d/\rho_g) = 10^{-2}$. For this setup, there is $\approx 225 M_{\oplus}$ of dust (excluding ices) located beyond $r = 20$ au at the beginning of the simulations.

2.2. Chemistry

Our focus is on understanding five major carbon and oxygen carrying molecules: H_2O , CO, CO_2 , CH_4 , and CH_3OH . These species have been chosen because together they represent the dominant carbon and oxygen-bearing species in the colder regions of the outer disk.

For these five molecules, we solve a set of (semi)analytical differential equations, which include the following CO processing pathways:

1. Successive hydrogenation of CO ice, ultimately leading to the formation of CH_3OH ;
2. CO reacting with OH on grain surfaces, leading to the formation of CO_2 ice;
3. Gas-phase CO reacting with He^+ , leading to the formation of CH_4 .

These pathways, and the details of how they are approximated here, are discussed more in Bosman et al. (2018b, Sect. 2.3) and Appendix A.

The initial abundances for the 5 species are listed in Table 1. These initial conditions are based on Bosman et al. (2018b, Table B.1), and correspond to the majority of the carbon being in CO, while the oxygen is initially split between CO and H_2O (see also Sect. A). For a discussion of the validity of these assumptions see Bosman et al. (2018b, Sect. B.4.2).

The timescales on which the chemical reactions take place is set by the cosmic ray ionization rate, which we set to $\zeta_{\text{CR}} = 10^{-17} \text{ s}^{-1}$ in our standard model. The surface densities we are interested in do not exceed 100 g/cm^2 ,

justifying the use of a constant ζ_{CR} (Umebayashi & Nakano 1981; Padovani et al. 2018). We do not include X-rays as a source of ionization, the presence of which could potentially speed up CO destruction in very low mass ($\leq 0.003M_{\odot}$) disks (Schwarz et al. 2018).

2.3. Freeze-out and desorption

Desorption energies for the 5 major species are listed in Table 1. The balance between freeze-out and desorption on small dust grains is assumed to reach steady state for all five major molecular species during each timestep (as in Bosman et al. 2018b). This is a valid assumption in most regions of the disk, but can potentially lead to the models underpredicting the amount of gas-phase CO in the cold outer disk regions, especially when these become depleted in dust (Semenov et al. 2006; Krijt et al. 2018). However, for the relatively weak turbulence strength used in this work, these effects will be minor. For pebble-size particles that drift through the midplane snowline, time-dependent sublimation is included, which will result in pebbles releasing CO molecules over an extended radial region (see also Piso et al. 2015).

For the initial abundances, the midplane CO snowline (defined as the location where 50% of the present CO is frozen out) is located at $r \approx 34$ au, where the midplane temperature equals $T(r) \approx 23\text{K}$.

2.4. Transport via turbulent diffusion

The evolution of solids is handled in way that is very similar to the approach described in Krijt et al. (2018), with small grains being treated as a fluid on a grid, while the dynamics of pebble-size particles are followed using a swarm of representative tracer particles.

For the small grains, the ices present on small grains, as well as trace gas-phase vapor species, diffusive transport is included using the approach of Krijt et al. (2018) (see also Ciesla 2009). The strength of the turbulence is controlled via the dimensionless α -viscosity parameter (Shakura & Sunyaev 1973), which is assumed to be connected to the gas diffusivity via $D_g = \alpha c_s H$. Motivated by Flaherty et al. (2015); Teague et al. (2016), we set $\alpha = 10^{-4}$, an order of magnitude lower than in the fiducial runs of Krijt et al. (2018).

2.5. Pebble formation and evolution

The formation and evolution of pebble-size particles is handled in way that is very similar to the approach described in Krijt et al. (2018). For increased flexibility and more control over the pebble behavior, however, we simplify the approach of Krijt et al. (2018, Sect. 3) in two ways:

1. We assume all pebbles that form in a single simulation have the same size s_p , independent of their formation location.
2. We approximate the dust-to-pebble conversion timescale as

$$\tau_{\text{d}\rightarrow\text{p}} = \frac{a_1}{\Omega} \left(\frac{\rho_{\text{d}}}{\rho_{\text{g}}} \right)^{-1}, \quad (1)$$

with Ω the local Keplerian frequency and a_1 a constant.

When pebbles form, they inherit the ice composition of the small grains present in that particular grid cell. The local abundance of small grains is lowered accordingly, and the effect of the decreasing small-dust-to-gas is included in the chemical network.

Vertical settling, radial drift, and turbulent transport are included following (Krijt et al. 2018). We include the sublimation of volatile species present on pebble-size particles if and when they move to disk regions with a higher temperature (i.e., as they drift inward), but otherwise pebbles are assumed to be chemically inert because of their small surface-to-mass ratio. In practice this means that small dust and pebbles can have quite different ice compositions, even when present at the same location.

In the fiducial model, we will set $s_p = 1$ mm throughout the disk and, as in Krijt et al. (2018), imagine further growth is frustrated by a combination of bouncing and radial drift removing particles before they can gain more mass. We ignore collisional fragmentation, which is reasonable for the outer disk regions and the fairly low value of $\alpha = 10^{-4}$ (Birnstiel et al. 2012; Misener et al. 2019). In more complex models, the exact maximum particle size is a function of location, local dust-to-gas ratio (for the drift limit), and particle composition, but a constant $s_p = 1$ mm suffices for our purposes and reproduces the typical pebble size outside ~ 20 au in more complete models to within a factor of a few (e.g., Stammerl et al. 2017; Krijt et al. 2018). For our disk model, pebbles of this size have Stokes numbers of $\text{St} = 4 \times 10^{-3}$, 0.02, and 0.05 in the midplane at $r = 20, 50,$ and 100 au, respectively.

2.6. Integration

Starting with all the dust present as sub-micron grains and the initial abundances listed in Table 1, the 5 molecular tracers (in either vapor and/or ice form), the small dust, and pebble tracers are evolved forward in time. During every iteration:

1. Gas-phase and grain-surface chemistry is advanced in each cell using the simplified scheme outlined in Appendix A.
2. The new sublimation and freeze-out balance is calculated and the partitioning of volatile species between ice and vapor is updated in each cell.
3. The exchange of small dust grains (carrying ices) and gas-phase species between neighbouring cells is calculated.
4. The positions of the pebble tracer particles are updated, taking into account vertical settling, radial drift, and turbulent diffusion.
5. The sublimation of ices carried by pebbles that have moved to warmer disk regions is calculated.
6. In each cell, a fraction of the locally available dust mass is stochastically converted into pebble particles. The ice on newly-formed pebbles has the same composition as the dust in that cell.

Steps 1–6 are repeated until $t = 3$ Myr have passed, and the timestep for this operative splitting routine is set by

TABLE 1
PROPERTIES OF MOLECULAR SPECIES
THAT ARE FOLLOWED.

Molecule	Initial abundance	E_{bind}/K
H ₂ O	1.2×10^{-4}	5770
CO	1.0×10^{-4}	855
CO ₂	1.0×10^{-5}	2990
CH ₃ OH	1.0×10^{-6}	4930
CH ₄	1.0×10^{-9}	1200

NOTE. — Desorption energies taken from [Bosman et al. \(2018b\)](#). Initial abundances in molecules per H.

the shortest diffusion timescale across a single cell ([Krijt et al. 2018](#), Eq. 17). Similarly, we set $a_1 = 10$, which results in coagulation timescales similar to those found in 1D models (see Sect. 3.3).

3. RESULTS

In this Section we describe increasingly complex models by adding physical and chemical processes one by one, as summarized in Table 2. Where possible, we compare the observed behavior to that seen in published studies that were similar in scope.

3.1. Static chemistry only

The starting point is a model in which we only include chemical processing and freeze-out/sublimation of molecular species. Dust coagulation and material exchange between adjacent grid cells is not included (see Table 2). The results of this model are presented in Fig. 2, in which the following locations, correspond (roughly) to the temperature and density combinations shown in Fig. 13, have been highlighted:

- A. Inside the CO snowline,
- B. Outside the CO snowline,
- C. Main freeze-out zone in the outer disk,
- D. The warm molecular layer (WML) (e.g., [Aikawa et al. 2002](#)).

The observed behavior can be directly compared to the chemically more sophisticated, but similarly static studies (e.g., [Walsh et al. 2010](#); [Henning & Semenov 2013](#); [Schwarz et al. 2018](#); [Bosman et al. 2018b](#), and others). Like [Schwarz et al. \(2018\)](#) and [Bosman et al. \(2018b\)](#), we find that the processing of CO in the warm molecular layer (e.g., location D) is inefficient on Myr timescales. In colder regions, where CO is either fully or partially frozen out on grain surfaces, more rapid processing can occur resulting typically in CO₂ ice (around $T \sim 20\text{--}25\text{K}$, see location A) and CH₃OH or CH₄ ice (where $T < 21\text{K}$, see locations B and C) becoming the dominant carbon carrier (see also Sect. 2.2 and [Bosman et al. 2018b](#), Figs. 5 and 7). Similar findings across a variety of disk temperature and density profiles led [Zhang et al. \(2019\)](#) to conclude that chemical processing alone is not an efficient way of removing the warm CO gas that dominates the emission readily probed by ALMA.

3.2. Chemistry and turbulent diffusion

The next step is to include material transport through turbulent diffusion. In the absence of dust coagulation, and thus large variations in the dust-to-gas ratio, abundance gradients are set mainly by spatial variations in temperature, gas density, and the radiation field. Generally, diffusion will act to smear out such spatial gradients in the concentrations of gas-phase and ice-phase species (e.g., [Willacy et al. 2006](#); [Ciesla 2009](#); [Semenov & Wiebe 2011](#)).

The timescale for vertical mixing to act on a scale Δx can be estimated as $t_z = (\Delta x)^2/D_g$. Focusing on vertical transport. For $\Delta x = H$ and assuming a diffusion coefficient based on a turbulence strength described by $\alpha = 10^{-4}$ (Sect. 2.1), we obtain $t_z \approx 0.25$ and 1.6 Myr at 30 and 100 au, respectively. These timescales are shorter than or comparable to the chemical processing in the disk midplane (Figs. 2 and 13), suggesting turbulent transport and chemical processing of CO are intertwined and the CO abundance is sensitive to transport processes.

The results of the chemistry and diffusion (DIFF) model are shown in Fig. 3. Comparing the behavior to the static CHEM model (Fig. 2), the effect of turbulent transport is indeed evident. First, the ice species produced near the midplane are effectively transported to the disk’s upper layers, resulting in CH₃OH and CH₄ being present at high z/H after 3 Myr. Second, the narrow band of CO₂ seen hugging the $T \sim 20\text{--}25\text{K}$ region in Fig. 2 has disappeared, with CO₂ ice only being the dominant carbon carrier for $r < 50$ au. In this region, however, fast vertical mixing has resulted in CO₂ being dominant throughout the entire vertical column. Qualitatively similar behavior has been found in earlier works by [Semenov & Wiebe \(2011\)](#); [Furuya & Aikawa \(2014\)](#).

Finally, Fig. 3 reveals a decrease in the gas-phase CO abundance in the WML of about an order of magnitude after 3 Myr. This can be understood in terms of vertical mixing: While local processing of CO in the WML is not efficient (see Fig. 2), the addition of diffusion allows gas-phase CO molecules to be cycled through the colder midplane, where (1) they rapidly stick to grain surfaces, and (2) can be processed to form less volatile species such as CH₃OH. These products, and the portion of CO ice that escaped processing, will eventually return to the WML, but overall the process is asymmetric and results in the loss of gas-phase CO from the upper regions on $\sim\text{Myr}$ timescales.

In the seminal work of [Semenov & Wiebe \(2011\)](#), the depletion of gas-phase CO in the outer disk was found to be inefficient (see also [Semenov et al. 2006](#)), its column density changing by no more than a factor $\sim 3\text{--}5$ over 5 Myr when turbulent diffusion was included. While a direct comparison is difficult because of several differences in the set-up (disk density and temperature structure, etc.), we attribute this difference to two reasons: (1) [Semenov & Wiebe \(2011\)](#) did not include H and H₂ tunneling. This results in a slower conversion of CO to CH₃OH on the grain surface, while making it easier to re-form CO as the incorporation of O into H₂O is also suppressed (see also [Bosman et al. 2018b](#)); and (2) [Semenov & Wiebe \(2011\)](#) used a ratio of diffusion to binding energy $E_{\text{diff}}/E_{\text{bind}} = 0.77$, substantially larger than our value of 0.3, also reducing the efficiency of grain sur-

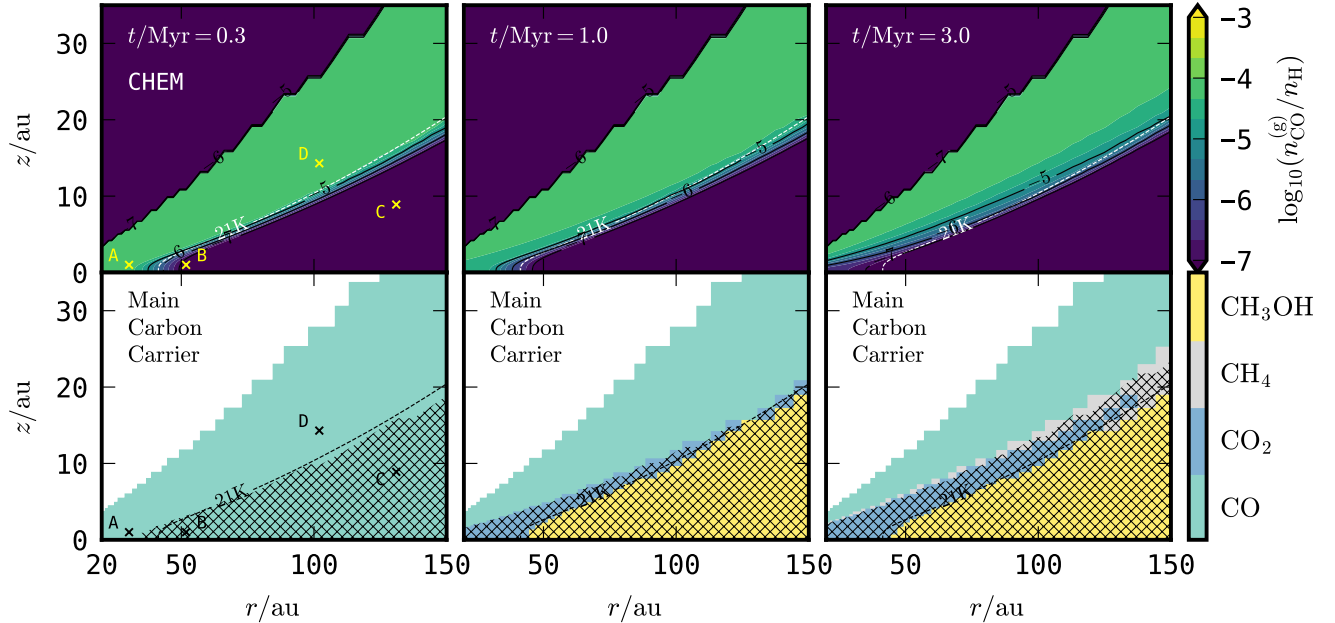


FIG. 2.— Snapshots of the evolution of the model including chemical reaction only (CHEM, see Sect. 3.1 and Table 2). Top: Gas-phase CO abundance as a function of location in the disk. Bottom: Main carbon carrier as a function of location in the disk. Shaded areas indicate the dominant carrier is present predominantly in solid form (i.e., frozen out on grain surfaces). The $T = 21$ K contour roughly indicates the location where CO transitions from being in the gas-phase (at higher temperatures) to being frozen out. Locations A, B, C, and D correspond to the temperature and density conditions shown in Fig. 13 in more detail.

TABLE 2
PROCESSES INCLUDED/EXCLUDED IN THE MODELS OF SECT. 3.

Model →	CHEM	DIFF	PEBB	FULL
Chemical processing	✓	✓	×	✓
Freeze-out/sublimation	✓	✓	✓	✓
Vapor diffusion	×	✓	✓	✓
Dust and ice dynamics	×	✓	✓	✓
Pebble formation & dynamics	×	×	✓	✓
Introduced in Figure	2	3	4	5

NOTE. — These models all employ $s_p = 1$ mm, $a_1 = 10$, and $\zeta_{CR} = 10^{-17}$ s $^{-1}$. Variations on the FULL model are presented in Sect. 4.

face chemistry.

3.3. Pebble formation and dynamics only

For completeness, we include here a model with dust evolution and transport only, without taking into account chemical processing (PEBB, Fig. 4). This set-up is essentially identical to the one used in Krijt et al. (2018), with the caveat that we have made several minor changes to the way the pebble size and coagulation timescale are calculated (e.g., Sect. 2.5).

As the result of pebble formation and vertical settling, the local dust-to-gas ratio decreases in the disk surface layer, and increases in the midplane (e.g., Krijt et al. 2018, Fig. 6). At the same time, the inward drift of pebble-size particles results in a radial mass flux of solids throughout the disk. Typically, at several 10s of au, this flux builds up rapidly, peaks around 10^5 yr, and then decreases slowly on $\sim 10^6$ yr timescales (Krijt et al. 2018,

Fig. 12), although the detailed behavior varies with location and depends on the (initial) disk properties and details of the dust coagulation process (e.g., Birnstiel et al. 2012; Lenz et al. 2019).

Figure 7 shows the time evolution of the total mass of various pebble reservoirs present in the PEBB simulation as well as the cumulative pebble mass that has drifted through the inner boundary. Over the course of the PEBB simulation, $\sim 220M_\oplus$ worth of pebbles can be seen to drift inward of $r = 20$ au, with about 10% of them doing so in the first 0.2 Myr. Pebble fluxes of similar magnitudes play an important role in modern planet formation theories, providing a means for planetary embryos to accumulate mass quickly through pebble accretion (Johansen & Lambrechts 2017; Ormel 2017). For example, roughly $\sim 150M_\oplus$ of pebbles are required to grow the cores of the solar system’s giant planets within 3 Myr (Lambrechts & Johansen 2014).

The consequences of pebble formation and dynamics on gas-phase CO abundances have been discussed in Krijt et al. (2018) and we recover the same behavior: (1) the CO abundance in the WML drops by a factor of a few as ices are sequestered on pebble-size particles in the midplane; and (2) the sublimation of rapidly-drifting and ice-covered pebbles results in a plume of gas-phase CO interior to the CO ice-line. The appearance of this plume will vary with time as the radial pebble flux evolves (see Fig. 7), while its shape and peak CO abundance depend sensitively on the strength of the turbulence and its relation to the diffusion coefficient (Stammler et al. 2017, Figs. 7 and 8).

3.4. Chemistry, pebble evolution, and diffusive transport

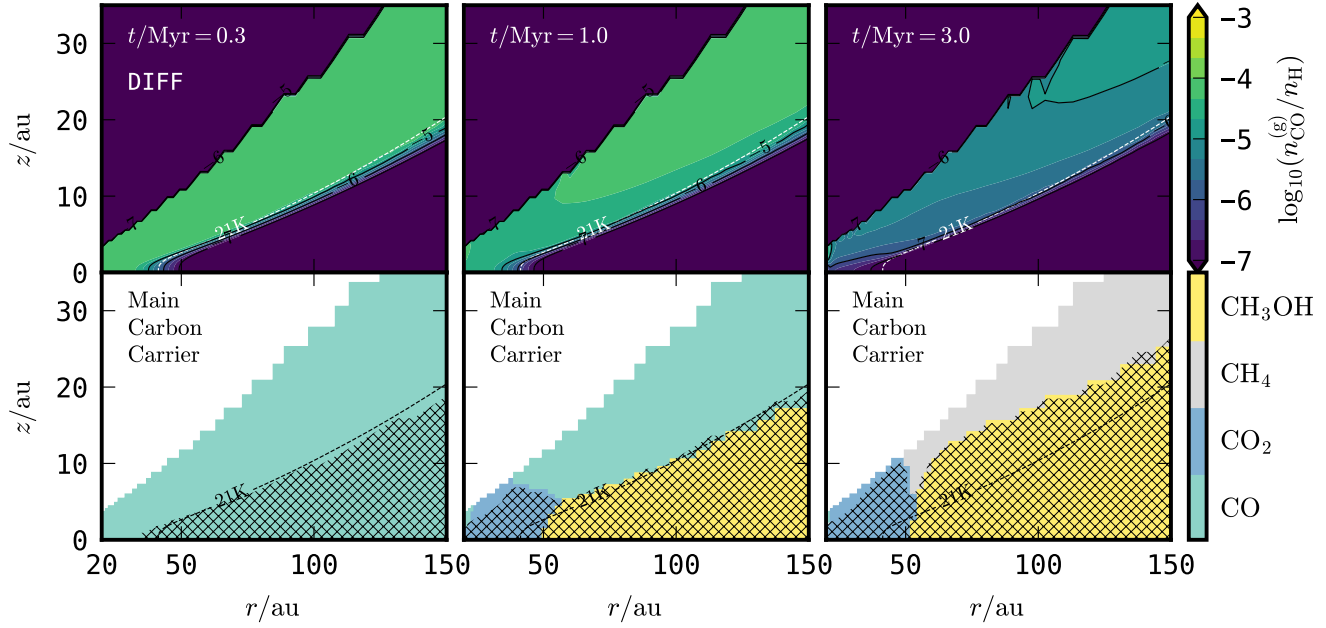


FIG. 3.— Snapshots of the evolution of the model including chemical reactions and diffusive transport of vapor and small solids (DIFF, see Sect. 3.2 and Table 2).

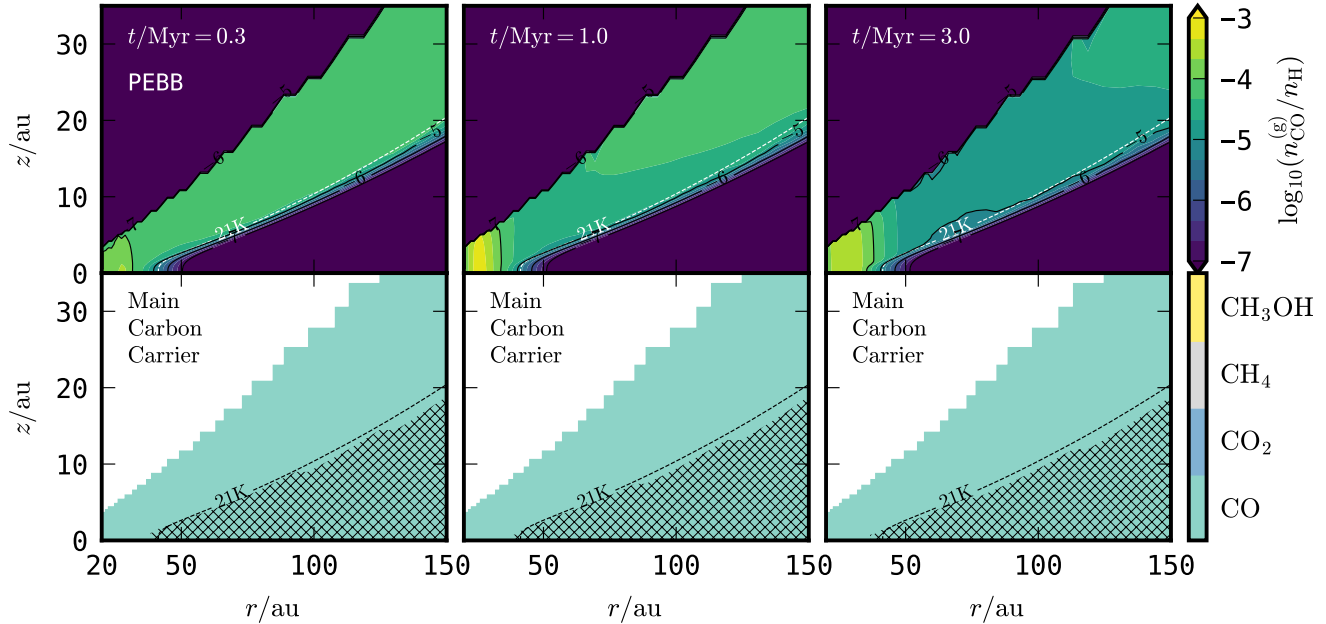


FIG. 4.— Snapshots of the evolution of the model including only dust coagulation and pebble migration (PEBB, see Sect. 3.3 and Table 2).

Finally, we present the results of the FULL model including chemistry, diffusive transport, coupled with dust coagulation and pebble dynamics in Fig. 5.

Since the processing of CO takes place on Myr timescales, the picture at early times (e.g., at 0.3 Myr) is comparable to the one presented in Fig. 4, with a similar plume of gas-phase CO developing centered around $r \sim 30$ au, and some CO disappearing from the WML around $r \sim 50$ au as it becomes sequestered on pebbles in the midplane. As in the PEBB model without chem-

istry, the plume inside the CO ice-line persists for 3 Myr, but the magnitude at the end of the simulation is significantly reduced. This can be seen clearly in Fig. 6, where we compare radial profiles of the gas-phase CO abundance (in the midplane and in the WML) for the 4 models described in Sects. 3.1-3.4. There are two reasons for this reduction. First, CO can be processed locally, mainly forming CO_2 at these pressures and temperatures (see Fig. 2). Second, as a result of chemical processing on grain surfaces, pebbles that form and arrive at the

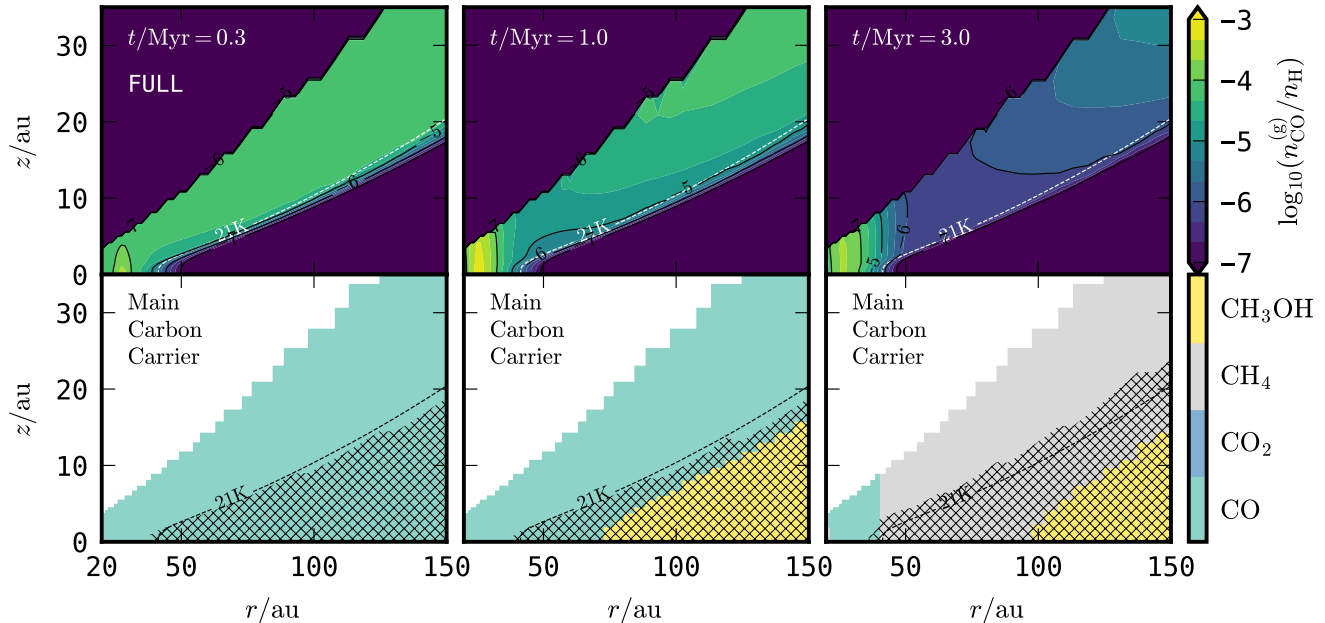


FIG. 5.— Snapshots of the most complete model presented here, which includes chemical reactions, dust coagulation, as well as material transport (FULL, see Sect. 3.4 and Table 2).

CO ice-line late in the simulation will carry a significant fraction of their carbon in the form of CH_3OH and CH_4 rather than CO (we come back to this point in Sect. 4.6). These species have their ice-lines further in, and will not be released to the gas-phase as these pebbles cross the CO ice-line.

In the region inside and around the CO ice-line, i.e., for $r < 50$ au, the inward migration and evaporation of CO -ice-coated pebbles results in gas-phase CO always being the dominant carbon carrier. The situation in the outer disk, however, especially for $t \gtrsim 1$ Myr, resembles more closely the picture presented in Fig. 3, with CH_4 and CH_3OH becoming the dominant carbon carriers. Focusing on the disk surface layer exterior to $r \sim 50$ au, we see that the two CO removal mechanisms encountered earlier (sequestration on pebble surfaces, and turbulent transport followed by chemical processing in the midplane) seem to exacerbate the depletion of gas-phase CO , with local abundances dropping by up to 2 orders of magnitude over the modelled 3 Myr. Such depletion factors are reached exclusively in the FULL model.

4. DISCUSSION

4.1. Pebble drift vs. chemical processing

In the framework presented here, there is nothing stopping pebbles from drifting inward in the models that include dust coagulation (Figs. 4 and 5). Thus, the only way to prevent a resurgence of gas-phase CO just inside the snowline from occurring is to have chemistry outpace pebble drift, resulting in pebbles carrying carbon in a less volatile form (i.e., in CH_4 and CH_3OH in our calculations). This is illustrated in the left panels of Fig. 8, where we have varied ζ_{CR} from 10^{-18} s^{-1} (FULL-CR18), 10^{-17} s^{-1} (FULL, the fiducial model), and 10^{-16} s^{-1} (FULL-CR16). We note that the overall ionization structure of disk systems as a function of time is

highly uncertain (e.g., Cleaves et al. 2013, 2015; Padovani et al. 2018) and the values used here represent a reasonable range for exploration. The pebble behavior has not been altered in these runs, so the flux of solids crossing the CO snowline is identical⁸ to the one depicted in Fig. 7. In the high cosmic ray model, the region with enhanced CO abundance around 20–40 au persists for less than a million years, with gas-phase CO being virtually absent after 3 Myr. The disappearance of the peak has 2 causes; (1) gas-phase CO is processed locally, mostly converted to CO_2 (see Sect. 3.1), and (2) chemical processing in the outer disk midplane means that pebbles arriving at times $t \gtrsim 10^5$ yr contain very little CO ice (see also Sect. 4.6 and Fig. 12).

Alternatively, the balance between chemical processing and radial drift can shift when pebble migration becomes less efficient or is completely halted. For example, the formation of larger bodies (i.e., planetesimals, see Sect. 4.6) or the trapping of pebbles in radial pressure bumps should reduce the radial pebble flux (e.g., Pinilla et al. 2020). In disks where massive planets have already formed, deep gaps in the gas surface density profiles can trap pebble-size particles outside the planet’s orbit with a near 100% efficiency (Pinilla et al. 2012; Bae et al. 2019). Indeed, pebble accumulations observed with ALMA (e.g., by the DSHARP survey) are regularly located exterior to the inferred CO ice-line (Huang et al. 2018; Long et al. 2018; Andrews 2020), clearly demonstrating the viability of trapping pebbles and the ices they carry in the outer regions of protoplanetary disks.

We illustrate the impact of these processes in the right-hand panels of Fig. 8, where we compare the fiducial model to a case where the drift efficiency is reduced by 90% (FULL-DR90), and 99% (FULL-DR99), respectively. It is evident that the CO depletion pattern in the outer

⁸ Not counting variations in their ice content.

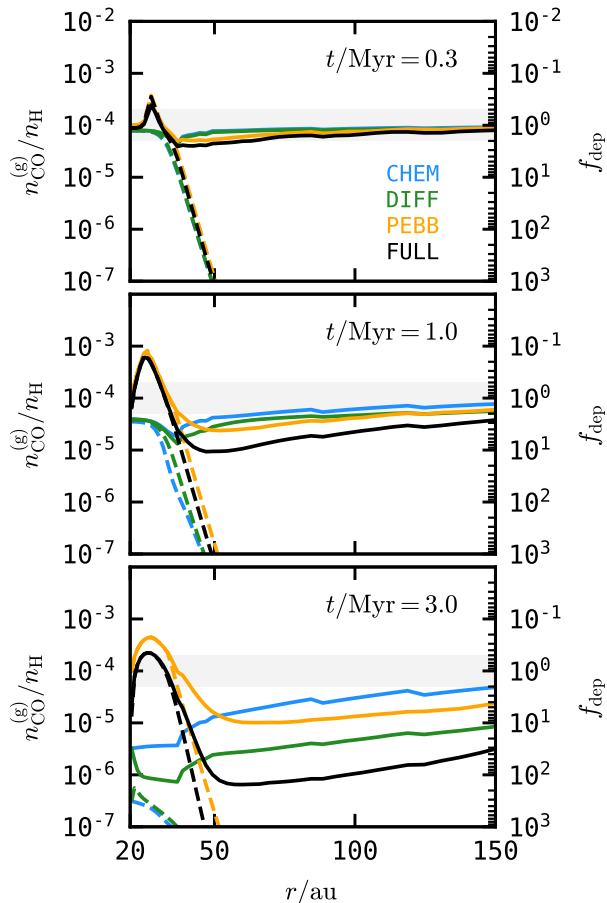


FIG. 6.— Radial profiles of the gas-phase CO abundance for the models presented in Figs. 2–5 as measured in the midplane (dashed curves) and the surface layer where $T > 21$ K (solid). The depletion factor f_{dep} indicates the fractional change in the gas-phase CO abundance relative to the initial value of 10^{-4} , and is most meaningful for the surface layer curves and the midplane region interior to the CO ice-line. The horizontal grey band shows values within a factor of 2 of the initial CO abundance.

disk WML is identical, as this is set mainly by vertical transport. The decreasing importance of radial motions for pebbles has a clear impact on the CO peak interior to the snowline. For the FULL–DR90 model, a small peak still develops, but it takes several Myr to do so. In the FULL–DR99 model, where pebble drift is essentially stopped (as would be the case when pebbles are converted to planetesimals very efficiently at all radial locations), even the region interior to the CO snowline becomes depleted in CO.

4.2. Comparison to Zhang et al. (2019, 2020b)

Recently, Zhang et al. (2019) derived radial profiles of the (gas-phase) CO depletion factor⁹ by combining spatially resolved CO isotopologue emission with SED modeling and thermo-chemical modeling for a handful of nearby disks (specifically, DM Tau, TW Hya, HD 163296, and IM Lup). While these disks vary in age, size, and temperature structure, we can qualitatively compare their findings to the results of our models.

⁹ The definition of the depletion factor is slightly different in this work, but in practice they are identical.

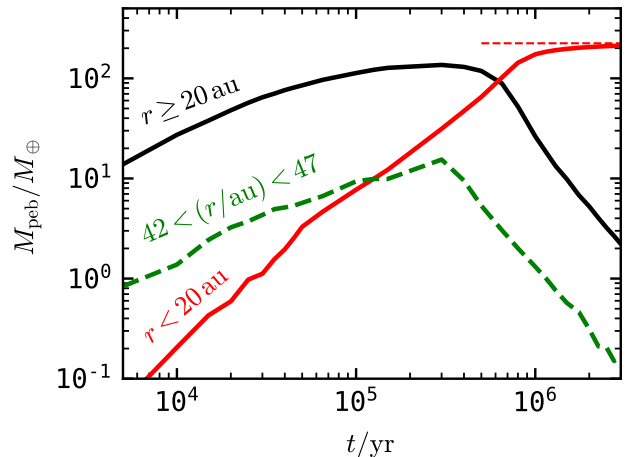


FIG. 7.— Total mass of pebbles formed in the PEBB and FULL models (Figs. 4 and 5) that: are still present in the simulation domain (solid black); are currently located between 42–47 au (dashed green); or have drifted interior to $r = 20$ au region (solid red). The thin red dashed line shows the initial solid content of the region >20 au.

Focusing on the WML region (solid curves) located beyond the CO ice-line, Fig. 6 indicates that depletion factors between ~ 10 – 100 , as inferred for IM Lup and TW Hya, are exclusively reached in the FULL model, which combined chemical processing with turbulent mixing and the sequestration of CO ice in the disk mid-plane. Even with these processes combined, however, several million years of evolution were needed to reach such severe CO depletion, while IM Lup is believed to be younger, ~ 1 Myr (Zhang et al. 2020a). Possible reasons for more rapid CO removal could include higher ionization rate (Fig. 8), higher turbulence in the disk surface layers (Xu et al. 2017; Krijt et al. 2018), or a colder disk in which the CO surface snowline lies further away from the midplane (Zhang et al. 2019, Fig. 4).

For HD 163296, the radial profile derived by Zhang et al. (2019) included the region just interior to the CO snowline, suggesting the presence of a plume of CO vapor, as predicted in our models that included pebble drift (Sects. 3.3 and 3.4) and earlier works by Stammer et al. (2017); Krijt et al. (2018). This local CO plume was further confirmed by the modeling of $^{13}\text{C}^{18}\text{O}$ (2–1) line spectrum of HD 163296 (Zhang et al. 2020b), who found that a radial pebble flux of ~ 15 – $60 M_{\oplus}/\text{Myr}$ is needed to reproduce the elevated C/H ratio interior to the CO snowline. Comparable fluxes¹⁰ are seen in our models that include pebble evolution (see Sect. 3.3). Observed substructure in the dust continuum emission of HD 163296 (e.g., Isella et al. 2018) might suggest efficient trapping of pebbles; however, Rosotti et al. (2020) argue that even the largest grains currently present in the disk are relatively well coupled to the gas, finding $(\text{St}/\alpha) \sim 20$ for the two rings firmly outside the CO snowline¹¹. Such observational constraints on the radial pebble flux are very valuable because this quantity plays a key role in shaping the final masses and orbital architectures of both

¹⁰ Note however that the number obtained in Zhang et al. (2020b) corresponds to the flux measured at 70 au.

¹¹ For comparison, the pebbles in the PEBB and FULL models have $(\text{St}/\alpha) \sim 200$ at $r = 100$ au.

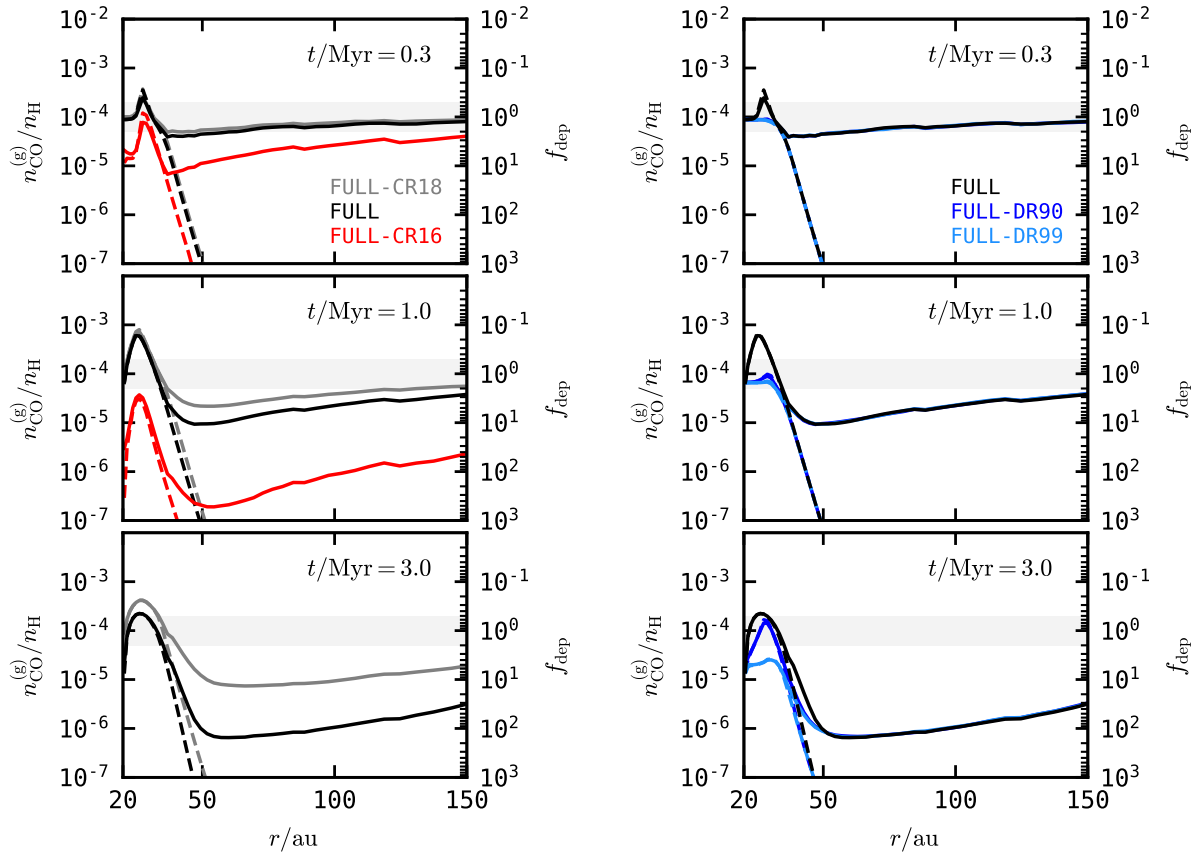


FIG. 8.— Impact on radial CO depletion profiles for varying cosmic ray ionisation rates ζ_{CR} (left) and pebble drift efficiencies (right). These models are discussed in Sect. 4.

gas giant and more terrestrial planets (e.g., [Johansen & Lambrechts 2017](#); [Lambrechts et al. 2019](#)). Lastly, the limited CO depletion in the outer disk for the relatively old HD 163296 are likely a result of the disk being fairly warm ([Zhang et al. 2019](#); [Dullemond et al. 2020](#)), rendering CO processing less efficient ([Bosman et al. 2018b](#); [Schwarz et al. 2018](#)).

For TW Hya, CO isotopologue emission reveals a significant amount of gas-phase CO between 5–20 au, with abundances significantly higher than in the outer WML, but still depleted relative to ISM levels ([Schwarz et al. 2016](#); [Zhang et al. 2017, 2019](#)). Recent studies by [Bosman & Banzatti \(2019\)](#) and [McClure & Dominik \(2019\)](#) also argue CO release inside 20 au is minimal, suggesting carbon is either transported inward in a different form, or that pebble migration has ceased altogether (see Sect. 4.1). However, as discussed in [Kama et al. \(2016, Sect. 6.3\)](#), the C/Si ratio of gas accreting onto TW Hya is an order of magnitude above that of typical T Tauri stars, suggesting that some carbon makes it to the inner disk even as refractory elements like Si are locked up in planetesimals or even larger bodies.

We note that while the disk used in this work was quite massive (see Sect. 2.1), we expect CO depletion to proceed similarly in lower mass disks as the relevant timescales do not depend on disk gas mass directly, but rather on the dust-to-gas ratio (for pebble formation) and the turbulence strength (for vertical mixing). Nonetheless, the detailed temperature structure and ionization

environment will set the timescale for chemical processing as well as the locations of snowlines. As such, in depth comparisons to observed protoplanetary disks warrant dedicated models for each individual object (e.g., [Zhang et al. 2019](#)).

4.3. Implications for disk mass estimates

In the absence of a direct gas mass tracer, gas-phase CO (isotopologue) line fluxes and dust continuum emission originating from the outer disk are frequently used to estimate disk gas masses. A common approach is then to assume ISM-like values for $\text{CO}/\text{H}_2 \approx 10^{-4}$ and/or $M_{\text{dust}}/M_{\text{gas}} \approx 10^{-2}$ (e.g., [Williams & Best 2014](#); [Miotello et al. 2016](#); [Ansdell et al. 2016](#); [Pascucci et al. 2016](#), and many others). Uncertainties in these indirect approaches have recently been discussed in e.g., [Bergin & Williams \(2017\)](#); [Kama et al. \(2020\)](#). Indeed, using an alternative method of looking at disk disk lines for several bright protoplanetary disks, [Powell et al. \(2019\)](#) obtain typical dust-to-gas ratios of $\sim 10^{-3}$ in the outer disk regions, and total gas disk masses between ~ 3 – $100\times$ higher than those derived from CO.

In our simulations, both the amounts of warm CO, dust, and pebbles vary significantly with time as a result of chemical processing and dust evolution. We illustrate the effects these processes can have on disk mass estimates in Fig. 9, which shows the time evolution of the mass-weighted CO/H_2 and solids-to-gas conversion factors for the various models shown in Fig. 8. The left panel

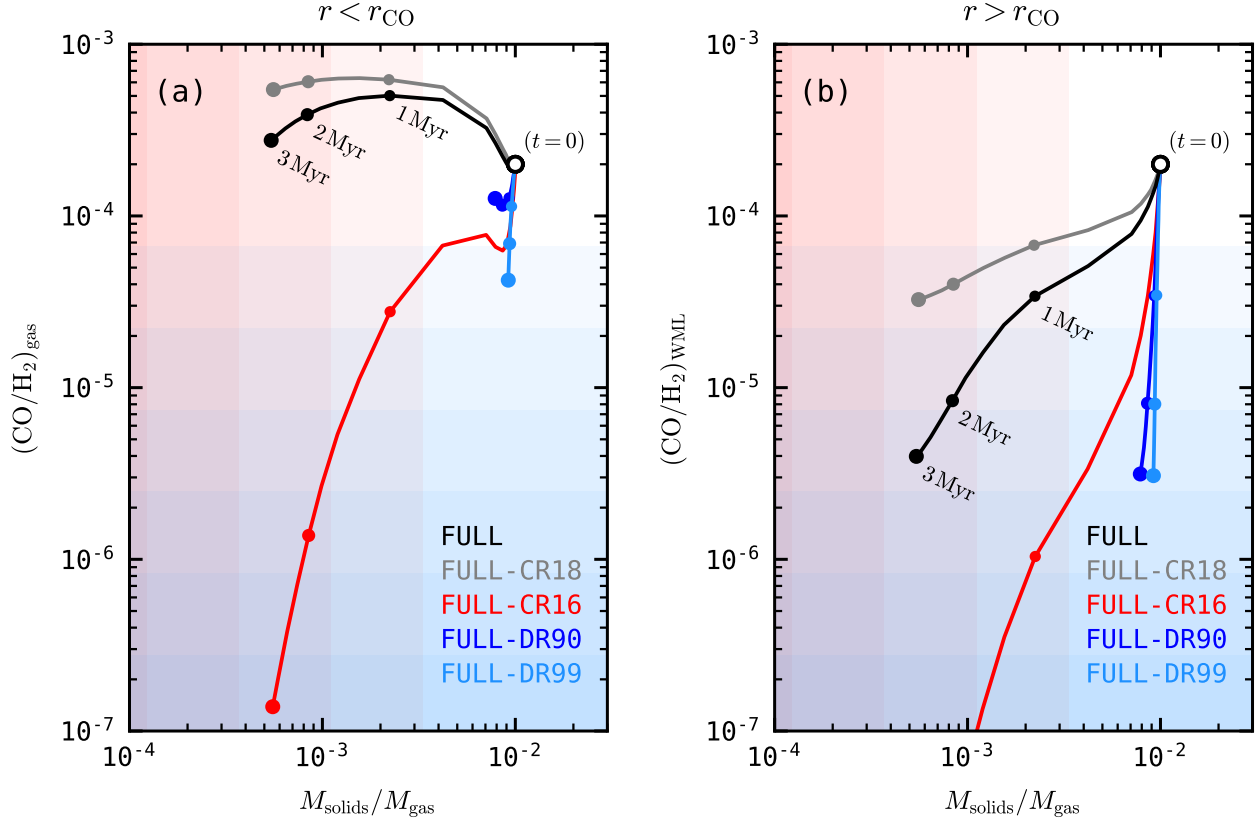


FIG. 9.— Evolution of the (mass-weighted) CO/H₂ in the gas inside the midplane CO snowline (left) and in the warm molecular layer (WML) outside the CO midplane snowline (right), compared to the total mass of solids (dust + pebbles) present exterior to $r = 20$ au (both panels). Background colors represent factors of 3× reductions in the CO abundance (blue) or solids-to-gas ratio (red).

shows warm CO interior to the midplane CO snowline, while the panel on the right illustrates the warm molecular layer in the outer disk. In both panels, horizontal axis represents the total (i.e., dust+pebble) solid-to-gas mass ratio integrated over the entire disk. Background colors represent factors of 3× reductions in the CO abundance (blue) or solids-to-gas ratio (red).

The trajectories depicted in Fig. 9 illustrate that the accuracy of using either CO emission (while assuming an ISM-like abundance) or dust emission (while assuming an ISM-like dust-to-gas ratio) as a total disk mass tracer depends sensitively on the details of the ongoing chemical and dust evolution. For example, in the FULL-DR90 and FULL-DR99 models, the reduced drift efficiency mean the the solid mass is hardly changing, while the warm CO in the outer disk drops by a factor $\sim 10^2$ over the modelled 3 Myr. In disks evolving in such a fashion, the dust mass would be a more reliable gas mass tracer, as found to be the case in the Lupus star forming region by Manara et al. (2016). Conversely, in the FULL-CR18 model (see Sect. 4.1), slow processing of CO and fairly rapid dust drift result in CO emission from the outer regions being a more reliable gas mass tracer (especially at times $\lesssim 3$ Myr), even if the CO/H₂ conversion factor has to be adjusted by a factor of a few. For the canonical FULL model, both the total solid and warm CO mass in the outer disk are reduced by over an order of magnitude in 3 Myr.

Generally, however, both the warm CO (at least in the outer disk) and total solid masses are decreasing func-

tions of time, implying that studies looking for evolutionary trends in gas disk masses by comparing star forming regions of different ages have to be careful when using CO/H₂ or dust-to-gas conversion factors that are constant in time, especially if a significant fraction of the disk mass is located beyond the CO snowline.

4.4. Elemental ratios and hydrocarbon production

The processes described in Sect. 3 will alter key elemental ratios in different ways. Recognizing that the effect of radial drift on gas and solid elemental abundances in the midplane has been discussed in detail by multiple authors (e.g., Cuzzi & Zahnle 2004; Ciesla & Cuzzi 2006; Estrada et al. 2016; Öberg & Bergin 2016; Booth et al. 2017; Booth & Ilee 2019), we focus here primarily on the warm molecular layer.

4.4.1. Gas-phase C/H and C/O

Figure 10 shows the gas-phase (C/H) and (C/O) ratios after 3 Myr for CHEM, DIFF, and FULL simulations. The behavior seen for (C/H)_{gas} largely follows the CO depletion pattern, as described for each simulation in Sect. 3 in more detail.

The story for (C/O)_{gas} is somewhat more involved. Initially, CO dominates the carbon and oxygen reservoirs in the gas, resulting in (C/O)_{gas} ≈ 1 at $t = 0$. As a result of chemical processing, this ratio tends to increase with time for the pressures and temperatures we are considering. The reason is that of the chemical products

considered here, CH_4 is the most volatile (after CO, see Table 1), its gas abundance pushing $(\text{C/O})_{\text{gas}} > 1$ as the more oxygen-rich products (e.g., H_2O , CO_2) readily freeze out. This effect is similar to the one described in Schwarz et al. (2019, Sect. 4.3.3), who reported $(\text{C/O})_{\text{gas}}$ as high as $\sim 10^8$ in the midplane at $r = 12$ au after 6 Myr, when virtually all CO had been processed.

In our simulations, the magnitude of the increase in $(\text{C/O})_{\text{gas}}$ and the extent of the region where it is seen depend on the transport processes that are included. In the static CHEM model (left panels of Fig. 10), only a relatively small region shows $(\text{C/O})_{\text{gas}} > 1$, since a significant fraction of the initial CO is still present after 3 Myr (see Fig. 2).

For the DIFF model, the combination of more efficient CO removal combined with the upward transport of CH_4 formed closer to the midplane results in a large portion of the WML having $(\text{C/O})_{\text{gas}} \sim 10\text{--}30$. There is a small region in the upper, inner part of the disk that has $(\text{C/O})_{\text{gas}} < 1$, due to sublimation of CO_2 that formed at lower temperatures and was subsequently transported there.

The FULL model also results in carbon-rich gas in the WML, but the increase is not as extreme as for the DIFF model without pebble formation and evolution. There are 2 reasons for this. First, in the inner disk, the enhancement in CO vapor interior to the CO snowline (see Sect. 3.4) dominates all other effects, forcing $(\text{C/O})_{\text{gas}} \approx 1$. Thus, if radial drift is taking place, we would not expect to see the extremely high (C/O) ratios in the inner disk midplane gas as found by Schwarz et al. (2019). Further out, say, in the WML between $r \sim 50\text{--}100$ au, the sequestration of a substantial amount of CH_4 ice on settled pebbles likely plays a role in the $(\text{C/O})_{\text{gas}}$ ratio being slightly lower than in the DIFF model, but still significantly $\sim 3\text{--}10$.

Designed to be focused on the processing of CO, the reduced chemical network we have used here does not consider further processing of CH_4 and the formation of other, generally less volatile, hydrocarbons. As such, the abundance of CH_4 at the end of our calculations, and the increase of $(\text{C/O})_{\text{gas}}$ associated with its appearance, should be treated as an upper limit.

4.4.2. Total volatile C/H and C/O

In models without dust coagulation and pebble dynamics, the total volatile (i.e., gas + ice) C/O ratio does not change with time, since there is either no transport between neighbouring cells (for the static CHEM model) or because the dynamics of gas-phase species and small ice-carrying grains are essentially identical (for the DIFF calculation). For these models, the initial concentrations described in Table 1 result in $(\text{C/O})_{\text{gas+ice}} \approx 0.5$ and $(\text{C/H})_{\text{gas+ice}} \approx 10^{-4}$ everywhere in the disk.

When dust evolution is included, however, the dynamics of carbon and oxygen can differ depending on how they are partitioned between gas and ice, leading to spatial and temporal variations in the total elemental ratios (e.g., Öberg & Bergin 2016; Booth & Ilee 2019). Figure 11 shows the total¹² volatile C/H and C/O ratios for

the FULL-CR18, FULL, and FULL-CR16 models (described earlier in Sect. 4.1).

The behavior shown by the $(\text{C/H})_{\text{gas+ice}}$ can be understood in terms of dust coagulation. As dust grows, especially in the regions exterior to the CO snowline, a significant amount of carbon gets locked up in pebbles, reducing $(\text{C/H})_{\text{gas+ice}}$ on a timescale comparable to pebble formation. This process is slightly less effective in the disk surface layers, where the carbon in CO and CH_4 is in the gas-phase. Inside the CO snowline, sublimation of inward drifting pebbles (e.g., Sect. 3.4) leads to a $(\text{C/H})_{\text{gas+ice}}$ ratio that is elevated by a factor $\sim 2\text{--}3$ compared to the initial value. For the FULL-CR16 model, the values for $(\text{C/H})_{\text{gas+ice}}$ in the inner regions are lower, as the more rapid chemical processing makes it easier for pebbles to carry away carbon in the form of CO_2 , and later CH_4 , ice.

The variations in $(\text{C/O})_{\text{gas+ice}}$ are caused by a mix of chemical processing and dust evolution, and can be understood as follows. In the cold outer disk midplane, virtually all carbon and oxygen are frozen out and $(\text{C/O})_{\text{gas+ice}} \approx (\text{C/O})_{\text{ice}}$. Even as pebbles form and leave this region, the remaining ice dominates the carbon and oxygen budget, leaving $(\text{C/O})_{\text{gas+ice}}$ relatively unaffected. In the surface layers, and inside and around the CO snowline, the picture is different. Here, initially, a significant amount of C and O are found in the gas, and the ice is generally more oxygen-rich than the gas, with the more volatile species (CO and CH_4) having $\text{C/O} > 1$. As the oxygen-rich ice is removed over time, $(\text{C/O})_{\text{gas+ice}}$ slowly increases, and even becomes > 1 as the abundance of CH_4 becomes comparable to that of CO. This happens faster in models with a higher ζ_{CR} , explaining the increasing $(\text{C/O})_{\text{gas+ice}}$ values going from FULL-CR18, to FULL, and FULL-CR16.

Elevated values $(\text{C/O})_{\text{gas+ice}}$ have been inferred from observation of multiple disks, with $(\text{C/O})_{\text{gas+ice}}$ ranging between 0.8 and 2.0 (Bergin et al. 2016; Cleeves et al. 2018; Miotello et al. 2019; Le Gal et al. 2019; Bergner et al. 2019). This is comparable to the range of values found in the FULL-CR18, FULL, and FULL-CR16 models. The models however, predict a strong correlation between CO abundance and $(\text{C/O})_{\text{gas+ice}}$ ratio in the surface layers, which so far has not been observed (Miotello et al. 2019). Again, the lack of further processing of CH_4 could lead us to over predicting the $(\text{C/O})_{\text{gas+ice}}$ in the top layers of the disk. Even so the dynamical and chemical processes studied here are at least in part responsible for the elevated $(\text{C/O})_{\text{gas+ice}}$ inferred from observations.

4.5. Implications for giant planet compositions

Following the seminal work of Öberg et al. (2011), many studies have sought to connect chemical abundances in the gas and solids, as found in the disk midplane, to the compositions of giant planet atmospheres (e.g., Öberg & Bergin 2016; Booth et al. 2017; Booth & Ilee 2019; Cridland et al. 2019). Recently, motivated by the theoretical and observational evidence that massive planets accrete gas primarily from the disk surface layers (Morbidelli et al. 2014; Szulágyi et al. 2014; Teague et al. 2019), Cridland et al. (2020) explored how gas accretion from reservoirs further up in the disk can alter the giant planet atmospheric composition, generally finding that

¹² Excluding contributions from pebbles, since these are found only very close to the midplane.

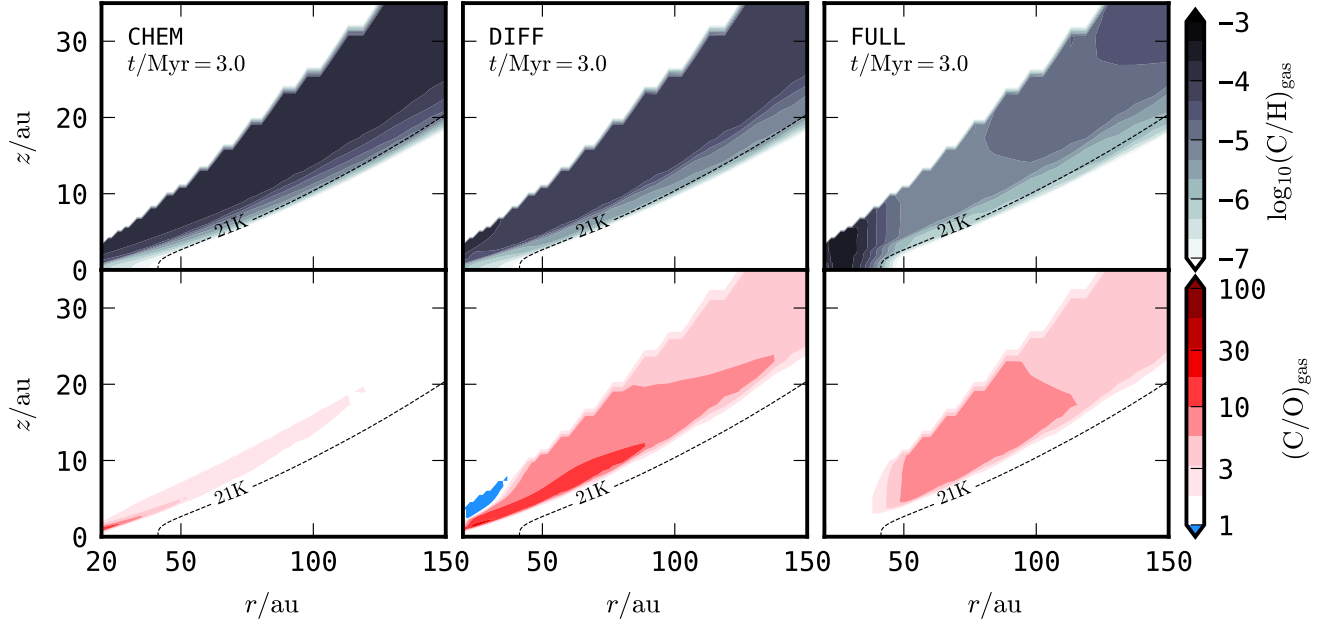


FIG. 10.— Gas-phase C/H (top) and C/O (bottom) ratios after 3 Myr for the CHEM (left), DIFF (middle), and FULL (right) models.

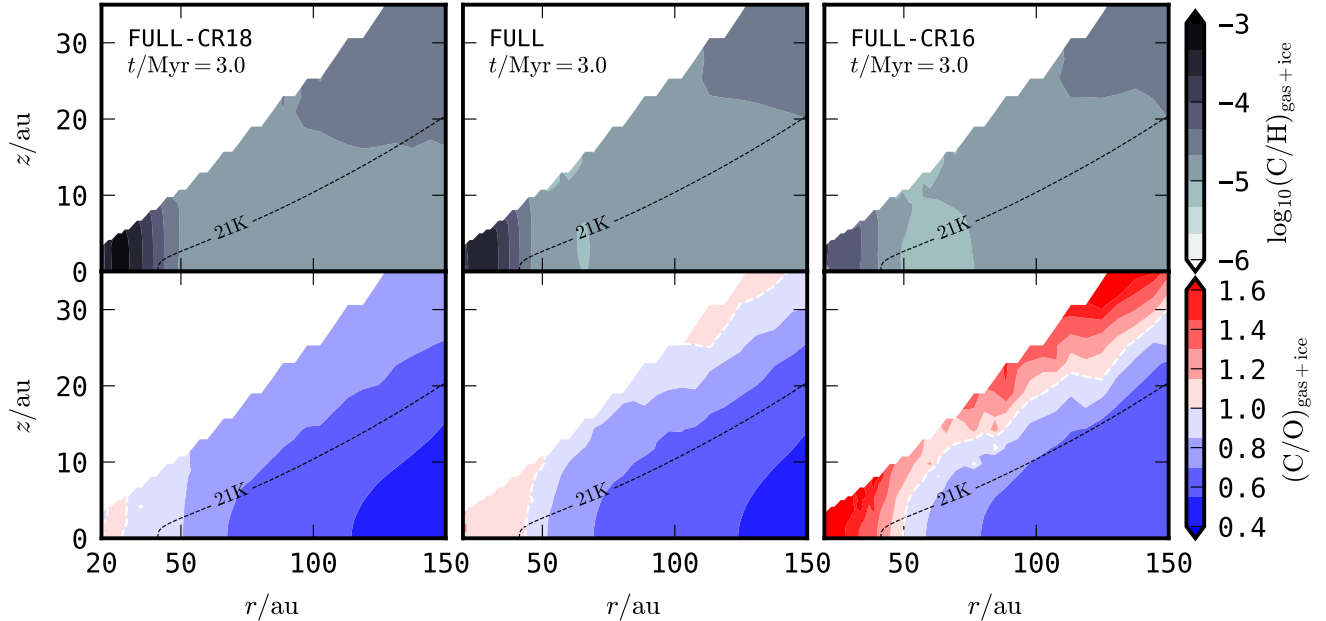


FIG. 11.— Total (gas+ice) C/H (top) and C/O (bottom) ratios after 3 Myr for the FULL-CR18 (left), FULL (middle), and FULL-CR16 (right) models. The white dashed line shows $(\text{C}/\text{O})_{\text{gas+ice}} = 1$. Note the different scales for the colorbar compared to Fig. 10.

the final C/O ratio was lower as the result of the accretion of oxygen-rich ices from between 1-3 scale-heights. The vertical profiles of the molecular abundances at the basis of the accretion model of Cridland et al. (2020) were based on otherwise static disk model. It would then be interesting to explore how the changes predicted here (e.g., Fig. 11) would impact the make-up of giant planets forming in the outer disk. However, only a relatively small fraction of the planet’s final mass was accreted from the disk surface layers, especially for planets that (start)

forming outside ~ 30 au (Cridland et al. 2020, Fig. 10). A more significant change in giant planet C/O ratios could come from the accretion of ice-rich pebbles in the disk midplane (e.g., Johansen & Lambrechts 2017). Understanding the balance between radial drift and chemical processing timescales (e.g., Sect. 4.1) is then key, as pebbles that carry processed carbon in the form of CH_3OH or CO_2 can hold on to their carbon for much longer than pebbles that are covered in more volatile CO ice.

4.6. Connection to CC-KBOs, (exo)comets, and interstellar interlopers

A more direct comparison can be made between the ice mantles in our simulations and the compositions of left-over planetesimals in the solar system and beyond. For example, [Eistrup et al. \(2019\)](#) recently compared constraints on cometary compositions to the time and location dependent ice abundances in their static chemical model, finding that the majority of cometary properties can be explained by a formation location in the vicinity of the CO ice-line.

The most direct connection is arguably possible for small bodies in the Cold Classical Kuiper Belt (CC-KB). This population of planetesimals, orbiting the sun between ~ 42 and 47 au on low-inclination, low-eccentricity orbits, is unique in that it contains some of the most pristine bodies in the solar system ([Priyalnik et al. 2020](#)). Moreover, the orbits of these bodies mostly undisturbed by the Neptune’s outward migration ([Nesvorný 2015](#)), suggesting their current location very close to their formation location. Finally, there is compelling evidence that these bodies formed through the gentle collapse of cloud of pebble-size particles concentrated via the streaming instability (e.g., [Nesvorný et al. 2019](#); [McKinnon et al. 2020](#)), implying that their bulk composition at the time of formation resembles closely that of the pebble precursors.

The best constraints on CC-KB object compositions come from the NASA New Horizons fly-by Arrokoth¹³ early in 2019 ([Stern et al. 2019](#)). While a body as small as Arrokoth cannot hold on to hyper-volatiles like CO ([Brown 2012](#)), a surprising finding was the clear detection of CH₃OH ice, coupled with a lack of strong H₂O ice features in the reflected NIR spectrum ([Grundy et al. 2020](#)). While it is unclear to what extent these surface features represent the bulk composition (see discussion in [Grundy et al. 2020](#)), we can attempt to compare these findings to results in our models.

Figure 12 shows the (mass-weighted) composition of all pebble particles present between 42–47 au (i.e., the location of the CC-KB) as a function of time for three models with different cosmic ray ionization rates. For the model with $\zeta_{\text{CR}} = 10^{-18} \text{ s}^{-1}$, grain surface chemistry is slow and the pebbles’ ice mantles are always composed of a large amount of CO ice, with $\lesssim 5\%$ CH₃OH ice. For the standard FULL model (middle panel), the highest concentration of methanol ice (relative to water ice) is reached after ~ 2 Myr. In the model with a high cosmic ray rate (right panel), a similar situation is reached already after ~ 0.4 Myr, after which the contribution of CH₃OH begins to diminish.

The current mass of the entire CC-KB population is estimated to be $\sim 3 \times 10^{-4} M_{\oplus}$ ([Fraser et al. 2014](#)), and region probably only suffered a factor of ~ 2 dynamical depletion during Neptune’s outward migration ([Nesvorný 2015](#)). Thus, even after 3 Myr in our simulations the region between 42–47 au contains enough mass in pebbles to produce a CC-KB like population of planetesimals (see Fig. 7).

Looking beyond the solar system, observations of second-generation CO gas (and its derivatives) in old

(>10 – 100 Myr) and otherwise gas-poor debris disks are being employed to constrain the combined CO+CO₂ mass fraction of planetesimals at the top of the collisional cascade ([Wyatt 2020](#), and references therein). For example, [Matrà et al. \(2017\)](#) constrain the combined CO+CO₂ ice mass fraction to lie between ~ 0.3 – 30% for the planetesimals in HD181327 and Fomalhaut. As these constraints become tighter and more systems are added, comparing such constraints to models like the ones presented here, and looking for trends with e.g., stellar luminosity or planetesimal belt location will undoubtedly provide valuable insights.

Lastly, interstellar interloper 2I/Borisov appears to be very rich in CO ice compared to solar system comets ([Bodewits et al. 2020](#); [Cordiner et al. 2020](#)), which has been taken as evidence for its formation exterior to the CO snowline. In the context of the models presented here, we would argue that, if indeed CO-rich, 2I/Borisov and the exo-comets in e.g. Fomalhaut not only formed exterior to the CO snowline in their systems, but also early during disk evolution, before significant processing of CO ice on grain surfaces took place.

We end by stressing that, in the simulations presented here, the local dust-to-gas ratio in the midplane is not readily enhanced sufficiently to result in planetesimal formation via the streaming instability (see also [Krijt et al. 2016, 2018](#)). It appears then that additional physics such as disk photoevaporation ([Carrera et al. 2017](#)) or the presence of (short-lived) pressure traps ([Lenz et al. 2019](#)) are needed to facilitate planetesimal formation outside of $r \gtrsim 10$ – 100 au.

5. SUMMARY

Motivated by recent observational constraints on the disappearance of gas-phase CO from the warm molecular layers of gas-rich protoplanetary disks ([Bergin & Williams 2017](#); [Zhang et al. 2019, 2020b,a](#)), we have self-consistently modeled the two sets of processes generally thought to be responsible: chemical processing ([Bosman et al. 2018b](#); [Schwarz et al. 2018](#)) and sequestration in the midplane ([Kama et al. 2016](#); [Krijt et al. 2018](#)).

Our main findings are as follows:

1. In our fiducial model with $\zeta_{\text{CR}} = 10^{-17} \text{ s}^{-1}$, chemical processing of CO combined with ice sequestration in the disk midplane, result in CO depletion factors of ~ 100 in the outer disk warm molecular layer after $t = 3$ Myr (Fig. 5).
2. Models that do not include chemical processing, dust coagulation and dynamics, or employ a lower cosmic ray ionization rate, do not reach similar depletion factors in the outer disk (Fig. 6 and 8).
3. Models that include pebble drift result in an enhanced CO abundance interior to the midplane CO snowline (Figs. 4, 5, and 6), unless chemical processing operates on timescales shorter than or comparable to disk-wide radial drift (Fig. 8).
4. Including chemical processing and dust dynamics results in elevated $(\text{C}/\text{O})_{\text{gas}} \sim 3$ – 10 in the warm molecular layer in the outer disk, while inward pebble drift and CO sublimation force $(\text{C}/\text{O})_{\text{gas}} \approx 1$ closer to the star (Fig. 10).

¹³ Formerly known as (486958) 2014 MU₆₉.

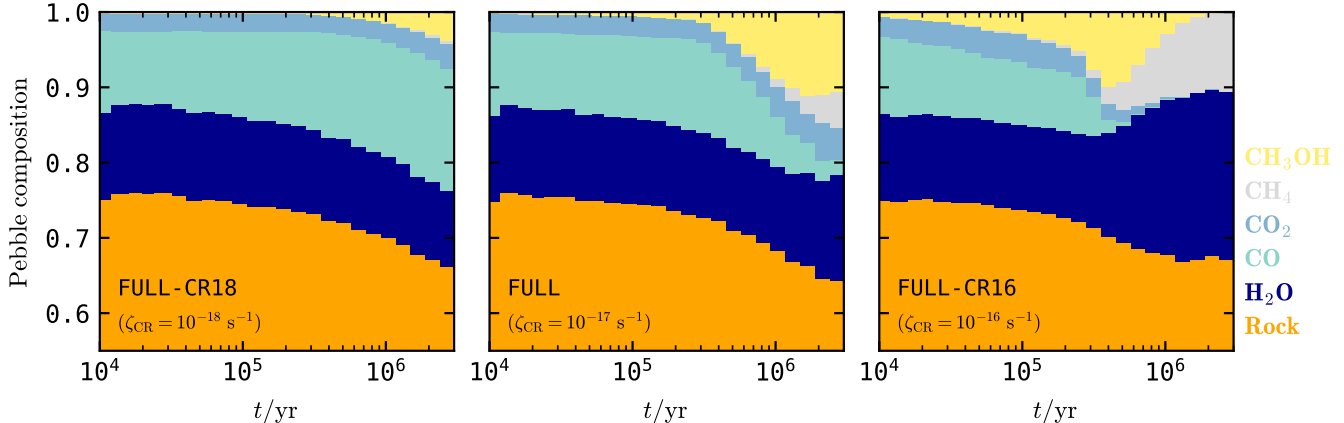


FIG. 12.— Normalized mass-weighted compositions of pebbles located between $r = 42$ and 47 au as a function of time, for the FULL-CR18, FULL, and FULL-CR16 models.

5. Dust evolution and material transport also alter the total volatile elemental abundances ratio, typically leading to $(C/O)_{\text{gas+ice}} \gtrsim 1$ inside the mid-plane CO snowline and parts of the warm molecular layer at larger radii (Fig. 11).
6. The removal of solids and warm CO from the outer disk on \sim Myr timescales complicates the use of their emission as a bulk disk mass tracer (Fig. 9).
7. Pebble compositions predicted by models like the ones presented here can be compared to knowledge of planetesimal compositions in the Kuiper belt and (extra-solar) comets to constrain the timing and location of their formation (Sect. 4.6), although planetesimal formation is not yet treated self-consistently in this work.

More broadly, our results highlight the need for studying the interplay between physical and chemical processes in gas-rich protoplanetary disks, and demonstrate

how molecular emission originating from the disk warm molecular layer can be used to constrain the growth and drift of solids in the disk midplane.

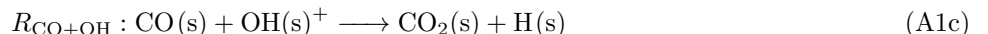
SK would like to thank Mihkel Kama, Ilaria Pascucci, Andrea Banzatti, Dmitry Semenov, and Dániel Apai for stimulating and encouraging discussions. SK, KZ, and KS acknowledge the support of NASA through Hubble Fellowship grants HST-HF2-51394.001, HST-HF2-51401.001, and HST-HF2-51419.001, respectively, awarded by the Space Telescope Science Institute, which is operated by the Association of Universities for Research in Astronomy, Inc., for NASA, under contract NAS5-26555. ADB acknowledges support from NSF Grant#1907653. The results reported herein benefited from collaborations and/or information exchange within NASA’s Nexus for Exoplanet System Science (NExSS) research coordination network sponsored by NASA’s Science Mission Directorate.

Software: matplotlib (Hunter 2007).

APPENDIX

A. REDUCED CHEMICAL NETWORK

In Bosman et al. (2018b) three pathways for the conversion of CO into other species have been studied using a full chemical network. As combining a full chemical network within a dynamical simulation is prohibitively expensive, we have created a reduced network that traces the major carbon carriers (CO, CO₂ and CH₃OH) as well as water and exhibits the same behaviour as the full chemical network in these species. Table 3 shows the reactions included in the reduced network. All the rates are calculated as in (Bosman et al. 2018b), and coefficients are taken from McElroy et al. (2013), Heays et al. (2017) and Garrod et al. (2008). All chemistry is ultimately driven by cosmic-rays, as such the cosmic-ray ionisation rate is critical parameter. More directly, CO conversion is dominated by three reactions¹⁴:



For reaction A1a, it is assumed that all carbon ends up as CH₄, while for reaction A1b, HCO is assumed quickly get further hydrogenated to CH₃OH. The abundances of He⁺, H(s) and OH(s) are thus necessary for the calculation of the evolution of the CO abundance. For each of these three species, we make the simplification that they are in equilibrium and that their abundance is thus given by equating the formation and destruction reactions for these species.

¹⁴ In the Appendix only, (s) is used to denote molecules/species frozen out on grain surfaces.

TABLE 3
REACTIONS INCLUDED

Reaction	Comments
$\text{H} + \text{H} \longrightarrow \text{H}_2$	H_2 grain surface formation according to Cazaux & Tielens (2004)
$\text{HX}(\text{s}) + \text{H}(\text{s}) \longrightarrow \text{X}(\text{s}) + \text{H}_2(\text{s})$	catalytic H_2 formation on the grains (Tielens & Hagen 1982)
$\text{X}(\text{s}) + \text{H}(\text{s}) \longrightarrow \text{HX}(\text{s})$	
$\text{H}_2\text{O}(\text{s}) + \gamma \longrightarrow \text{O}(\text{s}) + \text{H}(\text{s}) + \text{H}(\text{s})$	Cosmic ray induced photo dissociation (Heays et al. 2017)
$\text{CO}_2(\text{s}) + \gamma \longrightarrow \text{CO}(\text{s}) + \text{O}(\text{s})$	Cosmic ray induced photo dissociation (Heays et al. 2017)
$\text{CH}_3\text{OH}(\text{s}) + \gamma \longrightarrow \text{CH}_3(\text{s}) + \text{OH}(\text{s})$	Cosmic ray induced photo dissociation (Heays et al. 2017)
$n\text{H}_2 + 2n\text{CR} \longrightarrow 2n\text{H}$	H_2 dissociation due to cosmic rays efficiency n is between 2 and 4
$\text{He} + \text{CR} \longrightarrow \text{He}^+ + \text{e}^-$	Cosmic ray ionisation of He
$\text{He}^+ + \text{CO} \longrightarrow \text{C}^+ + \text{O} + \text{He}$	
$\text{He}^+ + \text{N}_2 \longrightarrow \text{N}_2^+ + \text{He}$	
$\text{He}^+ + \text{CH}_4 \longrightarrow \text{CH}_4^+ + \text{He}$	Reactions of He^+
$\text{O}(\text{s}) + \text{H}(\text{s}) \longrightarrow \text{OH}(\text{s})$	Hydrogenation of oxygen to OH, assumed to be instantaneous
$\text{CO}(\text{s}) + 4\text{H}(\text{s}) \longrightarrow \text{CH}_3\text{OH}(\text{s})$	Hydrogenation of CO, the initial step is assumed to be rate limiting
$\text{CO}(\text{s}) + \text{OH}(\text{s}) \longrightarrow \text{CO}_2(\text{s})$	CO_2 formation on the grain
$\text{OH}(\text{s}) + \text{H}(\text{s}) \longrightarrow \text{H}_2\text{O}(\text{s})$	H_2O formation on the grain
$\text{OH}(\text{s}) + \text{H}_2(\text{s}) \longrightarrow \text{H}_2\text{O}(\text{s}) + \text{H}(\text{s})$	H_2O formation on the grain
$\text{C}^+ + x\text{H}_2 + \text{e}^- \longrightarrow \text{CH}_x + x\text{H}$	Formation of CH_4 through
$\text{CH}_x \longrightarrow \text{CH}_x(\text{s})$	ion-molecule and hydrogenation
$\text{CH}_x(\text{s}) + (4-x)\text{H} \longrightarrow \text{CH}_4(\text{s})$	reactions

He^+ is only created by direct cosmic-ray ionisation of He and thus has a constant formation rate. He^+ is destroyed by reactions with gaseous CO, CH_4 and N_2 . The abundance for the first two species is tracked, while N_2 is assumed to be constant at an abundance of 10^{-5} w.r.t H.

The H(s) abundance is a bit more difficult to calculate. To get the abundance of H on the ice, the abundance of H in the gas-phase needs to be calculated first. In the gas-phase H is created by cosmic-ray ionisation of H_2 and subsequent reactions. Depending on the dominant pathway, between 2 and 4 H atoms are created after one H_2 ionisation. For the reduced network we use an average value of 2.4 H per H_2 ionisation which fits well with a broad range of conditions that are considered here. This reaction dominates the production Atomic H in the gas-phase. Atomic H get removed from the gas-phase, by the production of H_2 , for which we follow ([Cazaux & Tielens 2004](#)), and the freeze-out of H onto the dust grain. Balancing these rates gives an abundance for H in the gas-phase and thus a freeze-out rate of H. Sublimation of H is not included as the full chemical network predicts that more than 99% of the H that freezes out on the grains will react on the grain.

On the grain, atomic H can react with a number of species. Besides the reactions of H(s) with O, OH and CO, catalytic formation of H_2 on the ice is also considered using reaction of the form: $\text{XH}(\text{s}) + \text{H}(\text{s}) \longrightarrow \text{X}(\text{s}) + \text{H}_2(\text{s})$ and $\text{X}(\text{s}) + \text{H}(\text{s}) \longrightarrow \text{XH}(\text{s})$, where the former is the rate limiting step. In the full chemical network reactions of H with H_2S was the dominant pathway in most of parameter space. It is assumed that the $\text{H}_2\text{S}(\text{s})$ abundance is 2×10^{-8} . To calculate the H_2 formation rate, three times the rate of $\text{H}_2\text{S}(\text{s}) + \text{H}(\text{s})$ is assumed, to correct for the $\text{SH}(\text{s}) + \text{H}(\text{s})$ reaction as well as catalytic reactions with other species on the ice.

Finally the OH(s) abundance needs to be calculated. It is assumed that all O that is produced from the dissociation of CO, CO_2 and H_2O , is quickly turned into OH(s), further OH(s) is produced in the dissociation of $\text{CH}_3\text{OH}(\text{s})$. OH(s) can then react with H(s) and $\text{H}_2(\text{s})$, forming H_2O and CO(s), forming $\text{CO}_2(\text{s})$.

Calculating the abundances of these three key intermediate species allows for the calculation of the evolution of the four traced species, CO, CO_2 , H_2O and CH_3OH . As the evolution of these species is slow, and the abundance of the intermediate species only depends on the traced species, large times steps (in the order of kyr) can be taken in the computation of the chemical evolution. As the chemical times-scales speed up when the CO abundance drops, we stop the conversion of CO when its abundance is below 10^{-8} . Fig. 13 shows the comparison between the full chemical model and the approximate model for four different physical conditions. These are the same conditions as studied in [Bosman et al. \(2018b\)](#) and sample all CO conversion pathways.

REFERENCES

- Aikawa, Y., Miyama, S. M., Nakano, T., & Umebayashi, T. 1996, *ApJ*, 467, 684
- Aikawa, Y., van Zadelhoff, G. J., van Dishoeck, E. F., & Herbst, E. 2002, *A&A*, 386, 622
- Andrews, S. M. 2020, arXiv e-prints, arXiv:2001.05007
- Andrews, S. M., Wilner, D. J., Hughes, A. M., et al. 2012, *ApJ*, 744, 162
- Ansdell, M., Williams, J. P., Trapman, L., et al. 2018, *ApJ*, 859, 21
- Ansdell, M., Williams, J. P., van der Marel, N., et al. 2016, *ApJ*, 828, 46
- Bae, J., Zhu, Z., Baruteau, C., et al. 2019, *ApJ*, 884, L41
- Bergin, E. A., Cleeves, L. I., Crockett, N., & Blake, G. A. 2014, *Faraday Discussions*, 168, 61
- Bergin, E. A., Cleeves, L. I., Gorti, U., et al. 2013, *Nature*, 493, 644
- Bergin, E. A., Du, F., Cleeves, L. I., et al. 2016, *ApJ*, 831, 101
- Bergin, E. A. & Williams, J. P. 2017, *Astrophysics and Space Science Library*, Vol. 445, The Determination of Protoplanetary Disk Masses, ed. M. Pessah & O. Gressel, 1
- Bergner, J. B., Öberg, K. I., Bergin, E. A., et al. 2020, arXiv e-prints, arXiv:2006.12584
- Bergner, J. B., Öberg, K. I., Bergin, E. A., et al. 2019, *ApJ*, 876, 25
- Birnstiel, T., Klahr, H., & Ercolano, B. 2012, *A&A*, 539, A148
- Bodewits, D., Noonan, J. W., Feldman, P. D., et al. 2020, *Nature Astronomy*

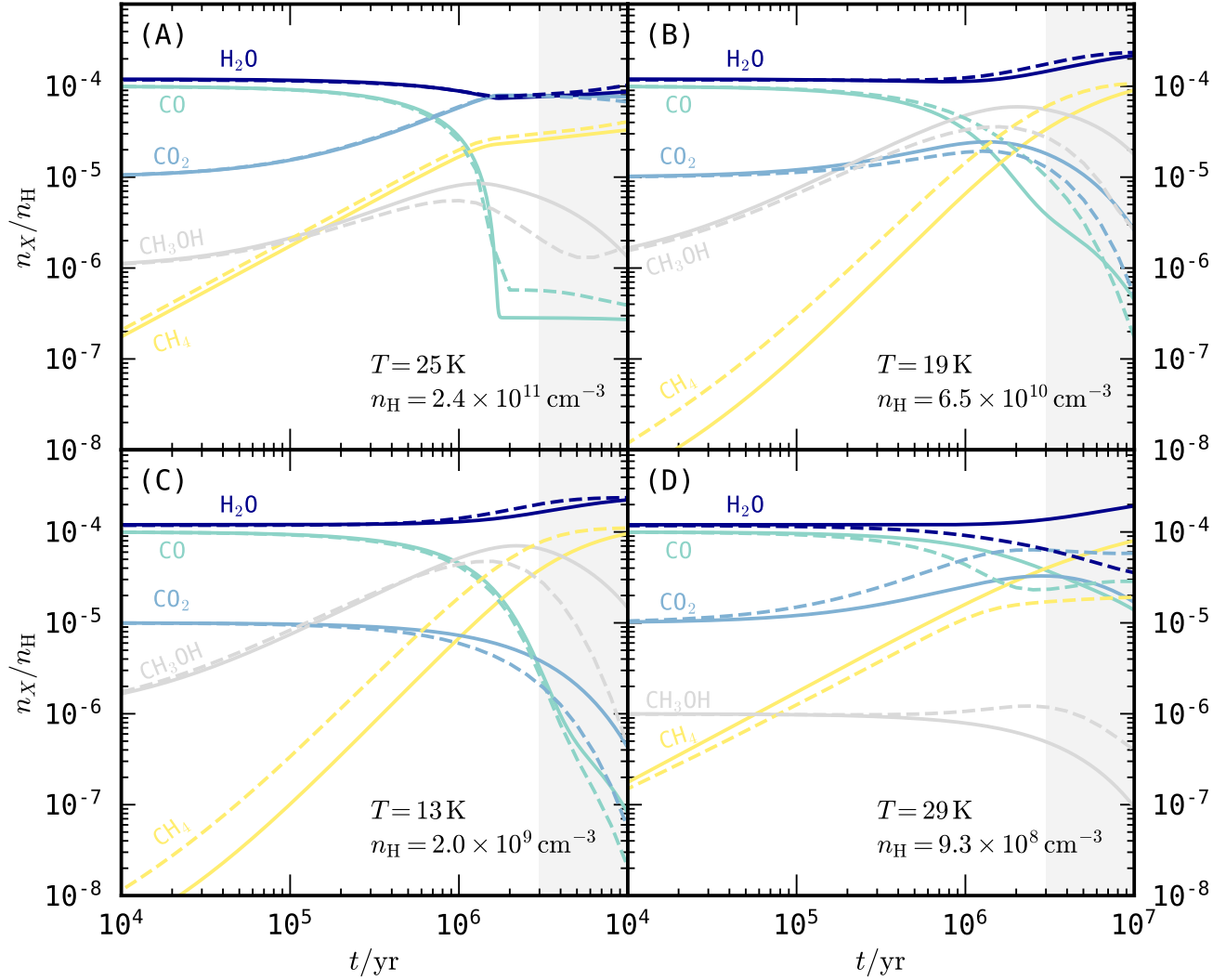


FIG. 13.— Comparison between the approximate model (solid) and the full chemical model (dashed), for four different combinations of gas temperature and density, corresponding (roughly) to locations A-D shown in Fig. 2. All curves show combined gas + ice abundances, for $\zeta_{\text{CR}} = 10^{-17} \text{ s}^{-1}$, a constant dust-to-gas ratio of 10^{-2} , and no grain growth. The grey area indicates times $t > 3 \text{ Myr}$. The approximate model closely follows the CO abundance as well as the abundance of the major carbon carrier, all within a factor of 2.

- Booth, R. A., Clarke, C. J., Madhusudhan, N., & Ilee, J. D. 2017, MNRAS, 469, 3994
- Booth, R. A. & Ilee, J. D. 2019, MNRAS, 487, 3998
- Bosman, A. D. & Banzatti, A. 2019, A&A, 632, L10
- Bosman, A. D., Tielens, A. G. G. M., & van Dishoeck, E. F. 2018a, A&A, 611, A80
- Bosman, A. D., Walsh, C., & van Dishoeck, E. F. 2018b, A&A, 618, A182
- Boyd, R. D. & Eisner, J. A. 2020, ApJ, 894, 74
- Brown, M. E. 2012, Annual Review of Earth and Planetary Sciences, 40, 467
- Carrera, D., Gorti, U., Johansen, A., & Davies, M. B. 2017, ApJ, 839, 16
- Cazaux, S. & Tielens, A. G. G. M. 2004, ApJ, 604, 222
- Ciesla, F. J. 2009, Icarus, 200, 655
- Ciesla, F. J. & Cuzzi, J. N. 2006, Icarus, 181, 178
- Cleeves, L. I., Adams, F. C., & Bergin, E. A. 2013, ApJ, 772, 5
- Cleeves, L. I., Bergin, E. A., Qi, C., Adams, F. C., & Öberg, K. I. 2015, ApJ, 799, 204
- Cleeves, L. I., Öberg, K. I., Wilner, D. J., et al. 2018, ApJ, 865, 155
- Cordiner, M. A., Milam, S. N., Biver, N., et al. 2020, Nature Astronomy
- Cridland, A. J., Bosman, A. D., & van Dishoeck, E. F. 2020, A&A, 635, A68
- Cridland, A. J., Eistrup, C., & van Dishoeck, E. F. 2019, A&A, 627, A127
- Cuzzi, J. N. & Zahnle, K. J. 2004, ApJ, 614, 490
- Dodson-Robinson, S. E., Evans, Neal J., I., Ramos, A., Yu, M., & Willacy, K. 2018, ApJ, 868, L37
- Dullemond, C. P., Isella, A., Andrews, S. M., Skobleva, I., & Dzyurkevich, N. 2020, A&A, 633, A137
- Dutrey, A., Guilloteau, S., Piétu, V., et al. 2017, A&A, 607, A130
- Eisner, J. A., Bally, J. M., Ginsburg, A., & Sheehan, P. D. 2016, ApJ, 826, 16
- Eistrup, C., Walsh, C., & van Dishoeck, E. F. 2018, A&A, 613, A14
- Eistrup, C., Walsh, C., & van Dishoeck, E. F. 2019, A&A, 629, A84
- Estrada, P. R., Cuzzi, J. N., & Morgan, D. A. 2016, ApJ, 818, 200
- Favre, C., Cleeves, L. I., Bergin, E. A., Qi, C., & Blake, G. A. 2013, ApJ, 776, L38
- Flaherty, K. M., Hughes, A. M., Rosenfeld, K. A., et al. 2015, ApJ, 813, 99
- Fraser, W. C., Brown, M. E., Morbidelli, A. r., Parker, A., & Batygin, K. 2014, ApJ, 782, 100
- Furuya, K. & Aikawa, Y. 2014, ApJ, 790, 97

- Garrod, R. T., Widicus Weaver, S. L., & Herbst, E. 2008, *ApJ*, 682, 283
- Grundy, W. M., Bird, M. K., Britt, D. T., et al. 2020, *Science*, 367, aay3705
- Heays, A. N., Bosman, A. D., & van Dishoeck, E. F. 2017, *A&A*, 602, A105
- Henning, T. & Semenov, D. 2013, *Chemical Reviews*, 113, 9016
- Huang, J., Andrews, S. M., Dullemond, C. P., et al. 2018, *ApJ*, 869, L42
- Hunter, J. D. 2007, *Computing in Science Engineering*, 9, 90
- Isella, A., Huang, J., Andrews, S. M., et al. 2018, *ApJ*, 869, L49
- Johansen, A. & Lambrechts, M. 2017, *Annual Review of Earth and Planetary Sciences*, 45, 359
- Kama, M., Bruderer, S., van Dishoeck, E. F., et al. 2016, *A&A*, 592, A83
- Kama, M., Trapman, L., Fedele, D., et al. 2020, *A&A*, 634, A88
- Krijt, S., Ormel, C. W., Dominik, C., & Tielens, A. G. G. M. 2016, *A&A*, 586, A20
- Krijt, S., Schwarz, K. R., Bergin, E. A., & Ciesla, F. J. 2018, *ApJ*, 864, 78
- Lambrechts, M. & Johansen, A. 2014, *A&A*, 572, A107
- Lambrechts, M., Morbidelli, A., Jacobson, S. A., et al. 2019, *A&A*, 627, A83
- Le Gal, R., Brady, M. T., Öberg, K. I., Roueff, E., & Le Petit, F. 2019, *ApJ*, 886, 86
- Lenz, C. T., Klahr, H., & Birnstiel, T. 2019, *ApJ*, 874, 36
- Long, F., Herczeg, G. J., Pascucci, I., et al. 2017, *ApJ*, 844, 99
- Long, F., Pinilla, P., Herczeg, G. J., et al. 2018, *ApJ*, 869, 17
- Manara, C. F., Rosotti, G., Testi, L., et al. 2016, *A&A*, 591, L3
- Matrà, L., MacGregor, M. A., Kalas, P., et al. 2017, *ApJ*, 842, 9
- McClure, M. K., Bergin, E. A., Cleeves, L. I., et al. 2016, *ApJ*, 831, 167
- McClure, M. K. & Dominik, C. 2019, *arXiv e-prints*, arXiv:1910.07345
- McElroy, D., Walsh, C., Markwick, A. J., et al. 2013, *A&A*, 550, A36
- McKinnon, W. B., Richardson, D. C., Marohnic, J. C., et al. 2020, *Science*, 367, aay6620
- Miotello, A., Facchini, S., van Dishoeck, E. F., et al. 2019, *A&A*, 631, A69
- Miotello, A., van Dishoeck, E. F., Kama, M., & Bruderer, S. 2016, *A&A*, 594, A85
- Miotello, A., van Dishoeck, E. F., Williams, J. P., et al. 2017, *A&A*, 599, A113
- Misener, W., Krijt, S., & Ciesla, F. J. 2019, *ApJ*, 885, 118
- Morbidelli, A., Szulágyi, J., Crida, A., et al. 2014, *Icarus*, 232, 266
- Nesvorný, D. 2015, *AJ*, 150, 68
- Nesvorný, D., Li, R., Youdin, A. N., Simon, J. B., & Grundy, W. M. 2019, *Nature Astronomy*, 3, 808
- Öberg, K. I. & Bergin, E. A. 2016, *ApJ*, 831, L19
- Öberg, K. I., Murray-Clay, R., & Bergin, E. A. 2011, *ApJ*, 743, L16
- Ormel, C. W. 2017, *Astrophysics and Space Science Library*, Vol. 445, *The Emerging Paradigm of Pebble Accretion*, ed. M. Pessah & O. Gressel, 197
- Padovani, M., Ivlev, A. V., Galli, D., & Caselli, P. 2018, *A&A*, 614, A111
- Pascucci, I., Testi, L., Herczeg, G. J., et al. 2016, *ApJ*, 831, 125
- Pinilla, P., Benisty, M., & Birnstiel, T. 2012, *A&A*, 545, A81
- Pinilla, P., Pascucci, I., & Marino, S. 2020, *A&A*, 635, A105
- Pinte, C., van der Plas, G., Ménard, F., et al. 2019, *Nature Astronomy*, 3, 1109
- Piso, A.-M. A., Öberg, K. I., Birnstiel, T., & Murray-Clay, R. A. 2015, *ApJ*, 815, 109
- Powell, D., Murray-Clay, R., Pérez, L. M., Schlichting, H. E., & Rosenthal, M. 2019, *ApJ*, 878, 116
- Prialnik, D., Barucci, M. A., & Young, L. 2020, *The Trans-Neptunian Solar System*
- Reboussin, L., Wakelam, V., Guilloteau, S., Hersant, F., & Dutrey, A. 2015, *A&A*, 579, A82
- Rosotti, G. P., Teague, R., Dullemond, C., Booth, R. A., & Clarke, C. 2020, *MNRAS*
- Schwarz, K. R., Bergin, E. A., Cleeves, L. I., et al. 2016, *ApJ*, 823, 91
- Schwarz, K. R., Bergin, E. A., Cleeves, L. I., et al. 2018, *ApJ*, 856, 85
- Schwarz, K. R., Bergin, E. A., Cleeves, L. I., et al. 2019, *ApJ*, 877, 131
- Semenov, D. & Wiebe, D. 2011, *ApJS*, 196, 25
- Semenov, D., Wiebe, D., & Henning, T. 2006, *ApJ*, 647, L57
- Shakura, N. I. & Sunyaev, R. A. 1973, *A&A*, 24, 337
- Stammler, S. M., Birnstiel, T., Panić, O., Dullemond, C. P., & Dominik, C. 2017, *A&A*, 600, A140
- Stern, S. A., Weaver, H. A., Spencer, J. R., et al. 2019, *Science*, 364, aaw9771
- Szulágyi, J., Morbidelli, A., Crida, A., & Masset, F. 2014, *ApJ*, 782, 65
- Teague, R., Bae, J., & Bergin, E. A. 2019, *Nature*, 574, 378
- Teague, R., Bae, J., Bergin, E. A., Birnstiel, T., & Foreman-Mackey, D. 2018, *ApJ*, 860, L12
- Teague, R., Guilloteau, S., Semenov, D., et al. 2016, *A&A*, 592, A49
- Tielens, A. G. G. M. & Hagen, W. 1982, *A&A*, 114, 245
- Trapman, L., Facchini, S., Hogerheijde, M. R., van Dishoeck, E. F., & Bruderer, S. 2019, *A&A*, 629, A79
- Umebayashi, T. & Nakano, T. 1981, *PASJ*, 33, 617
- Walsh, C., Millar, T. J., & Nomura, H. 2010, *ApJ*, 722, 1607
- Willacy, K., Langer, W., Allen, M., & Bryden, G. 2006, *ApJ*, 644, 1202
- Williams, J. P. & Best, W. M. J. 2014, *ApJ*, 788, 59
- Wyatt, M. 2020, *Extrasolar Kuiper belts*, ed. D. Prialnik, M. A. Barucci, & L. Young, 351–376
- Xu, R., Bai, X.-N., & Öberg, K. 2017, *ApJ*, 835, 162
- Zhang, K., Bergin, E. A., Blake, G. A., Cleeves, L. I., & Schwarz, K. R. 2017, *Nature Astronomy*, 1, 0130
- Zhang, K., Bergin, E. A., Schwarz, K., Krijt, S., & Ciesla, F. 2019, *ApJ*, 883, 98
- Zhang, K., Bosman, A. D., & Bergin, E. A. 2020a, *ApJ*, 891, L16
- Zhang, K., Schwarz, K. R., & Bergin, E. A. 2020b, *ApJ*, 891, L17